ESRF NEWSLETTER

High-pressure studies performed on ID30 provide evidence of a pressure memory signature in 3-D fullerene polymers produced at high temperature and pressure; "Debye-Scherrer Ellipses" have been observed *in situ* and in quenched samples indicating that the C_{60} cages contain a deformation due to compression which is retained at ambient pressure by the 3-D intermolecular bonding.

CONTENTS

Photography by:
G. Admans, C. Argoud and Jimagine.

USERS' MEETING

10/11 February 2000

The tenth ESRF Users' Meeting will take place on Thursday 10 February 2000 at the Atria conference centre. As usual the sessions will comprise reports on recent activities, highlight talks, posters and a commercial exhibition. In the evening there will be a dinner on-site at the ESRF.

Three workshops are planned for the one or two following days. Details, which are yet to be finalised, will be posted on the web. There will be a workshop on macromolecular crystallography and one on self organisation at interfaces and in thin films. The topic of the third workshop will be finalised shortly. Please consult the ESRF web pages (www.esrf.fr) for updated information.

M. Cooper

Workshop on X-ray Damage to Crystalline Biological Samples

9/10 June 1999

This Workshop was hosted by P. Lindley and attended by around 30 scientists from Europe and the U.S.A. The purpose of the workshop was to consider beam induced radiation damage and heating in macromolecular crystals undergoing structure determination by x-ray crystallography. The scope of the workshop, its format and the questions to be posed originated from discussions between E. Garman, C. Nave and G. Rosenbaum at conferences over the last 2 years.

With the advent of extremely intense x-ray beams from third generation synchrotron sources, observation of damage to cryo-cooled macromolecular crystals is becoming more common. In order to fully utilize the x-ray beams now available, some understanding of the processes involved in radiation damage and beam heating is required so that, if possible, evasive action to slow the damage rate can be taken.

At present, there is insufficient knowledge or understanding about radical production and diffusion in protein crystals in vitreously frozen solutions. More information is also required concerning radiation damage and beam heating and their relationship to incident dose, dose rate and incident wavelength. The workshop was convened to air all of these issues.

The workshop was informal and loosely structured to encourage maximum interchange of information and ideas. There were two main sessions, the first of which was to gather, collate and exchange information and to separate anecdotal evidence from fact. The second session was aimed at deciding on the most important questions to be answered experimentally, and then to apportion possible experiments to the various participating synchrotrons and laboratories on a complementary rather than competitive basis, since large amounts of beam time and effort are needed to obtain solid answers to the many open questions.

In the first session, two research teams [R. Ravelli (EMBL, Grenoble) and W. Burmeister (ESRF)] reported separate systematic studies on the effects of radiation decay in protein crystals. Talks followed which covered: damage in membranes and lipids [M. Caffrey (Ohio State)], current knowledge on dose rate versus overall dose effects and theoretical consideration of the temperature increase in a crystal [G. Rosenbaum (ANL)], modelling of the temperature rise in protein crystal during irradiation by finite element analysis [J. Nicolson (Daresbury)], factors to be considered when investigating radiation damage, and observations of damage to blue tongue virus crystals under different conditions [D. Stuart (Oxford)], damage to cryogenic biological samples in x-ray microscopy [D. Weiss (Gottingen)], a general overview of radiation damage and cryo methods for biological samples [C. Jacobsen (Stony Brook)], and a consideration of whether lowering the cryo-temperature to around 40K using helium as the cryogen could be expected to alleviate radiation damage effects [E. Garman (Oxford)]. Lively, yet focused discussion took place during and after these presentations.

In the second session the issue of collecting data at different wavelengths was addressed [A. Gonzales (EMBL Hamburg)] and the information from the first session was summarized [G. Rosenbaum (ANL)]. The experiments necessary to answer the questions require careful design, and are not trivial, since there are many convoluted variables. For instance, the same sized crystals should be used within each experiment for proper comparison. Four experiments were decided upon as the highest priority, the first aim being to determine the limiting dose above which samples decay very rapidly. This limit has been reported from observations at third generation synchrotron sources but additional controlled experiments are required. Participants agreed to attempt them before the next workshop, to be held in approximately a year's time.

P. Lindley brought the Workshop to a conclusion with a plea for more attention to be focused on designing and building faster detectors. Since it is likely that radiation damage rates can only be slowed, but not made insignificant, collecting the data in a shorter time would be the best option. Investment of money and resources are needed for further detector development.

E. Garman

A crystal of Salmonella typherium neuraminidase which has been irradiated at 100 K for 19 hours in a bright synchrotron beam. It was then allowed to warm up in cryo-buffer. The irradiated part of the crystal has completely disintegrated as a result of the released radiation damage products. The remaining L-shaped piece of crystal was re-cooled to 100 K and it still diffracted to beyond 1.0 Å.

Biological Crystal Characterization Workshop:
"identifying what a good biological crystal is"

10/11 June 1999

This workshop brought together scientist from several communities, mainly concerned with macromolecular crystallography, crystal growth and crystal characterization (with special emphasis on x-ray diffraction imaging, "topography"). The convening of the workshop corresponds with the fact that, associated with the progress in crystal growth techniques, the mosaic spread of many biological crystals has decreased dramatically over the last few years: such that the measured x-ray diffraction rocking curves from lysozime crystals are currently only a few arc seconds wide.

The topic of the workshop was introduced by P. Lindley and summarized, substantially, in the first transparency of the introductory talk by R. Fourme, who simply asked "what is a good biological crystal?"

At least two answers emerged from the contributions to the workshop:

1) from the macromolecular crystallography point of view a good crystal is the one which allows us to reach a better resolution, i.e. the smallest interreticular lattice plane distance d_{min}, as clearly explained by R. Fourme himself.

2) from the x-ray characterization point of view a good crystal displays a small mosaic spread, and few images of defects and distorted regions in the topographs, as illustrated by the curves and images presented by M.-C. Robert, F. Otalora, A. Aubry and V. Stojanoff.

The correlations between these two approaches were discussed in a lively way. R. Fourme showed, with the help of a simple model, that d_{min} should be proportional to σ, the static Debye-Waller factor which characterizes the crystal static disorder (defects, mosaic spread, etc.).

Of course the smaller σ is, the more perfect the corresponding crystal. The proportionality factor between d_{min} and σ is a function of the experimental conditions (detector, signal-to-noise ratio, etc.) and is being decreased by the use of third generation synchrotron radiation sources.

The experiments roughly confirm this approach for relatively deformed crystals: reducing the mosaic spread of the samples, from say 10^{-1} to 10^{-2} degrees, entails a big improvement in the resolution. This is not so evident when dealing with the best crystals, which exhibit a mosaic spread smaller than 10^{-2} degrees. However, in practice, this is not usually the case because of the damage caused by freezing and radiation.

The size and quality of the crystals results primarily, as explained by A. Tardieu, from the protein surfaces adequacy for crystallization, which varies dramatically from one protein to the other. Additionally, size and quality are a function of the growth conditions, and several new approaches allow further enhancement of these properties: growth in a gel or an electric field (A. Aubry) or under microgravity, or by reducing the growth rate. The topographic diffraction images performed on these crystals show features which look very much like the usual defects in inorganic crystals (growth striations, growth sectors and even dislocations). **Figures 1** and **2** show examples of topographs from biological crystals. Unfortunately both the very nature of these features and the mechanisms by which they produce a contrast allowing their observation (which were discussed by B. Tanner when describing the techniques allowing characterization of these crystals) are still unclear.

The participants at the Workshop agreed, after an interesting discussion, that we are still in a preliminary stage of the work in this topic. A summary of the conclusions resulting from the discussion is as follows: **a)** the current knowledge about the defects present in biological crystals is still poor and should be improved **b)** the relationship between the observed defects and the 'resolution' of the structure is not straightforward, and should be considered as a long term project and **c)** these topics are worth continued investigation, through a joint effort of the various teams concerned with and using the x-ray diffraction and imaging techniques described by
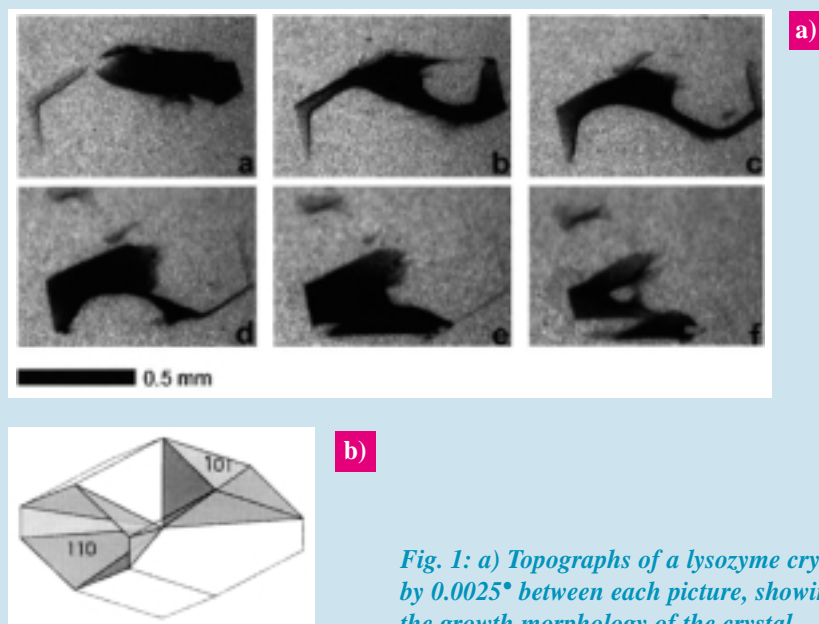

Fig. 1: a) Topographs of a lysozyme crystal recorded at different θ values, and rotated by 0.0025° between each picture, showing the different growth sectors. b) Scheme of the growth morphology of the crystal.
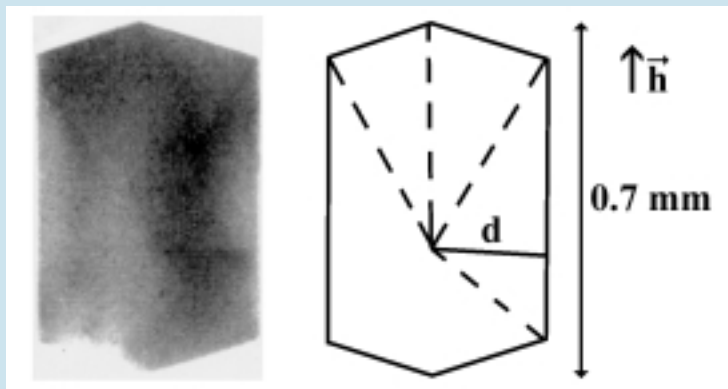
4

Fig. 2: Topograph of a chicken egg lysozyme crystal grown in silica showing the growth sectors. $\vec{h}$ is the diffraction vector.

B. Tanner. This should include systematic experiments to clearly identify the features observed on the topographs, and *in situ* experiments (growth, freezing, dehydration, radiation damage). P. Siddons (psiddons@bnl.gov) and J. Härtwig (haertwig@esrf.fr) were requested to co-ordinate this effort.

J. Baruchel

WORKSHOP ON PIXEL DETECTORS

17/18 June 1999

A workshop on so-called "pixel detectors" was held on 17 and 18 June at the ESRF, bringing together 17 invitees representing the most advanced teams working on pixel detector development in Europe and the United States. Opened by Y. Petroff, this workshop organized by H. Graafsma, C. Ponchut (ESRF Instrument Support Group), P. Lindley, C. Kunz, and C. Bassani (ESRF Experiments Division) was attended by about sixty people, both from inside and outside of the ESRF. The aim of the workshop was to introduce the state of the art in pixel detector development as well as to discuss possible applications at the ESRF.

But what is a pixel detector? It can be defined roughly as a matrix of independent x-ray detection channels each one having its own signal processing circuits, all put together on one silicon chip. The presentations demonstrated that this concept could actually provide significant enhancements over currently used CCD-based x-ray detectors. For example, having more than 16 bits dynamic range and less than 10 ms readout time, they are able to meet some of the requirements expressed by S. Wakatsuki for protein crystallography and T. Narayanan for small angle scattering. Detailed

insights into detector design showed how it could also bring along several new features such as shutterless acquisition and coarse energy discrimination, thereby opening the way to a completely new field of experiments. New crystallographic data acquisition strategies such as fine phi slicing were proposed and discussed, in order to exploit these novel detector features. Examples of applications with evaluation results were presented for powder diffraction, medical imaging and spectroscopy, illustrating the number of possible implementations. Some matters of concern were not hidden but extensively discussed, such as radiation hardness and how to build large areas by stitching

together small unit modules.

As a conclusion it was agreed that several x-ray analysis techniques, among which SAXS, PX and time-resolved diffraction, could actually benefit from this technology as soon as detectors with larger area become available. Additional test experiments on unit detector modules will be carried out at the ESRF in order to fully assess pixel detectors on an experimental basis.

The organizers are specially indebted to the speakers for the quality of their twenty presentations, as well as to the ESRF staff for its active and efficient support, which resulted in a lively and successful event.

C. Ponchut

31ST COUNCIL MEETING

7 and 8 June 1999

The Council

• discussed the future of the Multiple Wavelength Anomalous Dispersion beamline (**BM14**), in particular the options

- of maintaining BM14 in operation in view of an expected further increase in the demand for the MAD technique and

- of selling BM14 to a Collaborating Research Group or transforming it into an industrial beamline with a view to recuperating part of the ID29 expenditure for the beamline refurbishment budget,

and encouraged Management to explore further the feasibility of these options and have them discussed by the Science Advisory Committee at its next meeting;

• took note of the developing position with regard to the implementation of the law on the reduction of working time to **35 hours** and to the revision of the *Convention d'Entreprise* (collective agreement) and discussed the aspects of funding compensatory measures in particular;

• approved (with the German delegation abstaining or dissenting for some items)

- the revision of the **1999 budget** and

- **the Medium-Term Financial Estimates (2000-2004)** including the planning figure for Members' contributions to the budget of 2000 (= 404 MFF),

as proposed by the Management;

• adopted a statement on **industrial policy**;

• noted the **scientific use** of the ESRF made by each Contracting Party from 1994 to 1998 and discussed the reasons and the possible remedies for the imbalances found.

The council made the following appointments:

• P. Zinsli (Switzerland) as its Chairman for the period January 2000 to December 2001;

• H. Weijma (Benesync) as Chairman and B.L. Bye (Nordsync) as Vice-Chairwoman of the Administrative and Finance Committee / Audit Committee for the period July 1999 to June 2001;

• H. Fuess (TH Darmstadt) Chairman and J. Bordas (Laboratori de Leum Sincrotró, Barcelona) Vice-Chairman of the Science Advisory Committee;

• J. Bordas, G.H. Lander and D. Stuart as members to the Standing Committee on Permanent Appointments, in addition to the two *ex officio* members (Chairman of the SAC, Vice-Chairman of the Council).

K. Witte

PUBLIC HEALTH MEASURES IN THE ESRF/ILL GUEST HOUSE

Two users who stayed in the Guest House during the first half of the year (one in February, the other in May) have contracted Legionnaires' Disease. Although a causal link between the stay in the Guest House and these cases of illness has not been proven, Management, after being informed of the first case, immediately undertook preventive measures and ordered tests. Legionnaires' Disease is caused by exposure to water aerosols polluted by a bacterium which may be present in water networks and air conditioning systems. Evidence of contamination has been found in some shower heads of buildings A and B of the Guest House which in itself is not too surprising since these bacteria can be found in practically all water systems, particularly in stagnating warm water such as in shower units not regularly used.

Disinfection measures were carried out in July, which included: removal of calcium deposit from the heat exchangers, a heat shock treatment of the hot water network in buildings A and B, and a replacement of all shower heads, flexible hoses and the ceramic parts of the mixing batteries. After a series of tests for contamination had been carried out, all three buildings of the Guest House were again made available for use after the summer shut-down period (ie. from 12 August onwards).

In parallel, the ESRF has contacted all persons who arrived at the site from the 1 June onwards and who stayed in building A or B of the Guest House. They were informed of the problem and were asked whether they had any health problems subsequent to their visit to Grenoble. Fortunately no further cases have been reported.

For the future, preventive measures such as thermal shocks in all three buildings (twice a year), systematic monitoring of the legionella level and regular flushing of water in unused rooms will be implemented.

K. Witte

"Debye-Scherrer Ellipses": A Giant Anisotropic Deformation in C_{60} Polymers at High Pressure and High Temperature

M. Mezouar[1], L. Marques[2], J.-L. Hodeau[3], M. Núñez-Regueiro[4]

1 ESRF, Experiments Division
2 Departamento de Física, Universidade de Aveiro, Aveiro (Portugal)
3 Laboratoire de Cristallographie, CNRS, Grenoble (France)
4 Centre de Recherches sur les Très Basses Températures, CNRS, Grenoble (France)

"Debye-Scherrer Ellipes" provide evidence of a giant anisotropic deformation in C_{60} polymers, produced under elevated temperature and pressure conditions, which may be retained at ambient pressures.

Since C_{60} became available to researchers in the solid state and in suitable quantities, there have been predictions of possible interconnected fullerene lattices with interesting properties. Such phases would result in denser and more saturated species having a more pronounced sp3 character and they would allow the building of new host structures, based only on a pure carbon framework. High pressure studies have determined the existence of 1-D and 2-D polymer structures, made up of C_{60} molecules attached through 2+2 cycloaddition bonds. More recent x-ray synchrotron radiation measurements performed at the ESRF have demonstrated the existence of a 3-D arrangement of polymerized fullerene molecules. Ellipsoidal x-ray Debye-Scherrer diffraction patterns, the signature of a giant anisotropic deformation, have been observed during *in situ* and quenched experiments at high pressure and high temperature. This unusual effect, related to the process of deformation of the C_{60} cages during the compression, is retained at ambient pressure by 3-D intermolecular bonding or released in the case of low-dimensional polymers.

POLYMERIC STRUCTURES

Fullerene molecules, like other non-saturated systems, have been shown to polymerize either photochemically or under high pressure and high temperature (HP-HT) [1-2]. Molecular rotation is needed for the photo-polymerization to be accomplished, and it probably occurs at random. Little is known about the photopolymer structure because its x-ray diffraction pattern presents broad peaks centered at fcc lattice positions, corresponding to a slightly contracted cell in comparison with the monomer cell. Conversely, high pressure and high temperature (HP-HT) yields C_{60} structures consisting of ordered arrays of polymerized C_{60} molecules. X-ray diffraction studies have shown that these polymeric structures are, depending on the pressure-temperature conditions of preparation, either one-dimensional (1-D), two-dimensional (2-D) or three-dimensional (3-D) implying a polymerization reaction that proceeds along some preferred directions and not at random.

In the 1-D polymer, the C_{60} molecules are linked into polymeric chains while in the 2-D polymers they form hexagonal or square polymerized layers (Figure 1). In the 3-D polymer, the molecular bonding occurs in the twelve nearest neighbor directions. Synchrotron radiation powder diffraction using a fast image plate detector was first performed on quenched 3-D C_{60} polymerized samples. Structural analysis of diffraction patterns have shown that this 3-D polymer exhibits unusual ellipsoidal Debye-Scherrer diffraction patterns [3]. This unusual effect is illustrated in Figure 2. 1-D diffraction profiles taken on an arbitrary azimuthal direction of these spectra can be perfectly indexed on a fcc fullerite compressed lattice whose cell parameter varies continuously with the angle of azimuth.
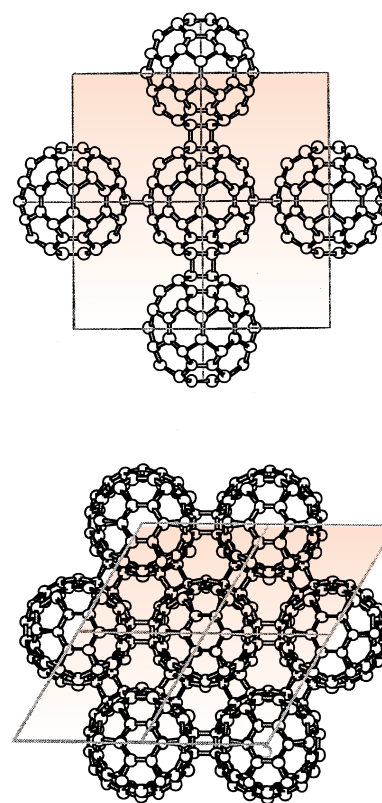

Fig. 1: Examples of (2+2) inter-molecular bonding occurring in 2-D fullerite polymers.

IN SITU ANALYSIS

This effect has been extensively studied *in situ* at high pressure and high temperature in the Paris-Edinburgh setup of ID30 (Figure 3) which has previously been described in detail [4]. A typical diffraction pattern obtained at P = 2 GPa and T = 473 K using this setup is presented in Figure 4. It was evident that the *in situ* diffraction pattern exhibits the
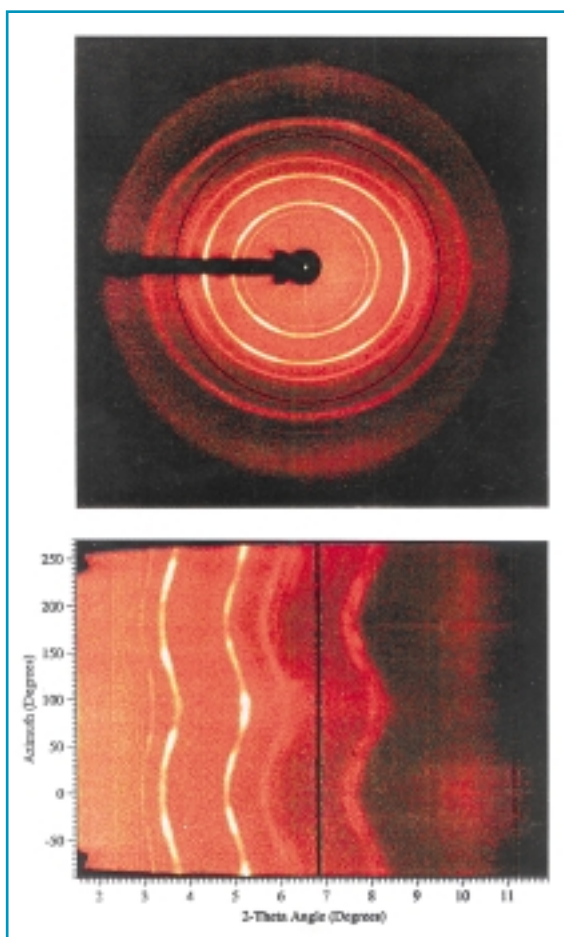
Fig. 2: Diffraction image and the corresponding unrolled projection along an azimuthal angle (an entire ring corresponds to 360° variation of the azimuthal angle) of the 3-D C60 polymer (from [3]).

compounds other than fullerenes, such an effect is much smaller (ellipsity < 1%) and is only observed *in situ* at high pressure.

A HUGE ELLIPSITY

In contrast, the fullerene ellipsity can be huge (up to 9%) and retained in quenched samples. As the compressed polymerized fullerite samples have been produced in non-hydrostatic conditions, we must conclude that the inter-molecular bonding is capable of "freezing" the stress gradient under which these phases are prepared. The orientation of the uniaxial stress is unique in the bulk sample and, depending on its orientation relative to that of the x-ray beam, different anisotropic patterns are observed.

One can add that the systematic *in situ* investigation of the p-T phase diagram of C_{60} in the Paris-Edinburg press has shown a much more complex behavior than previously admitted. Indeed, depending on the p-T path, and not only on the p-T values of the synthesis, the phase transformations can be significantly different. For instance, when the polymerization initiates in the orientationally ordered state, ordered structures of C_{60} are formed. While, when the polymerization initiates in the orientationally disordered state, the polymerization takes place at random and an isotropic polymer is formed, giving rise to fcc patterns as it is for photo-polymerized fullerites.

This study demonstrates the ability of the large volume press in the *in situ*

same elliptical shape as that of the quenched 3-D polymer. The continuous loci of the Bragg reflections in Figure 4 are elliptical and not circular, as expected for normal powder Debye-Scherrer patterns obtained with a 2-D detector placed perpendicular to the beam axis. These ellipsoidal patterns are due to the deviatoric stress that results from the

uniaxial character of the force that was used to establish the pressure. The elliptical shape results from a larger compression of the crystallographic lattice parameters in the direction of the applied force, as the magnitude of each inter-reticular distance d_{hkl} is a function of its orientation with respect to the stress field within the sample. On
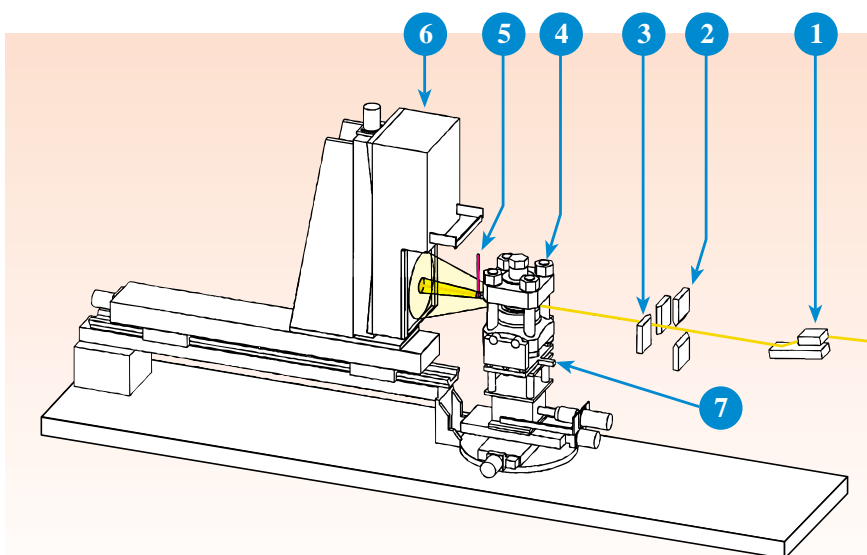

Fig. 3:
Layout of the High Pressure beamline ID30 at the ESRF in large-volume press configuration.
1: Si(111) channel-cut monochromator, 2-3: Tungsten carbide slits, horizontal and vertical limits, 4: Paris-Edinburgh large-volume press, 5: Beam stop, 6: Fast-scan, 7: Press holder.

synchrotron diffraction studies for low-Z elements. Depending on the p-T path used for the synthesis of fullerite polymers, a continuous range of phase transformations can be reached, from disordered to ordered phases and from 1-D to 3-D phases. This latter phase is likely to be a continuous network of mainly sp3 carbon atoms with large cages placed periodically, that is a carbon zeolite. Furthermore the Debye-Scherrer "ellipses" and the large anisotropic deformation observed on C_{60} indicate that this material can support, visualize and memorize large uniaxial stresses. ■

REFERENCES

[1] A.M. Rao, P. Zhou, K.A. Wang, G.T. Hager, J.M. Holden, Y. Wang, W.T. Lee, X.X. Bi, P.C. Eklund, D.S. Cornett, M.A. Duncan, I.J. Amster, Science, **259**, 95 (1993).

[2] Y. Iwasa, T. Arima, R.M. Fleming, T. Siegrist, O. Zhou, R.C. Haddon, L.J. Rothberg, K.B. Lyons, H.L. Carter Jr., A.F. Hebard, R. Tycko, G. Dabbagh, J.J. Krajewski, G.A. Thomas, T. Yagi, Science, **264**, 1570 (1994). M. Nunez-Regueiro, L. Marques, J.L. Hodeau, O. Bethoux, M. Perroux, Phys. Rev. Lett., **74**, 278 (1995).

[3] L. Marques, M. Mezouar, J.L. Hodeau, M. Nunez-Regueiro, N.R. Serebryanaya, V.A. Ivdenko, V.D. Blank, G.A. Dubitsky, Science, **283**, 1720 (1999).

[4] M. Mezouar, T. Le Bihan, Y. Le Godec, H. Libotte, M. Thoms, D. Häusermann, Paris-Edinburgh large volume cell coupled with a fast imaging plate system for structural investigation at high pressure and high temperature, accepted for publication in J. Synch. Rad.
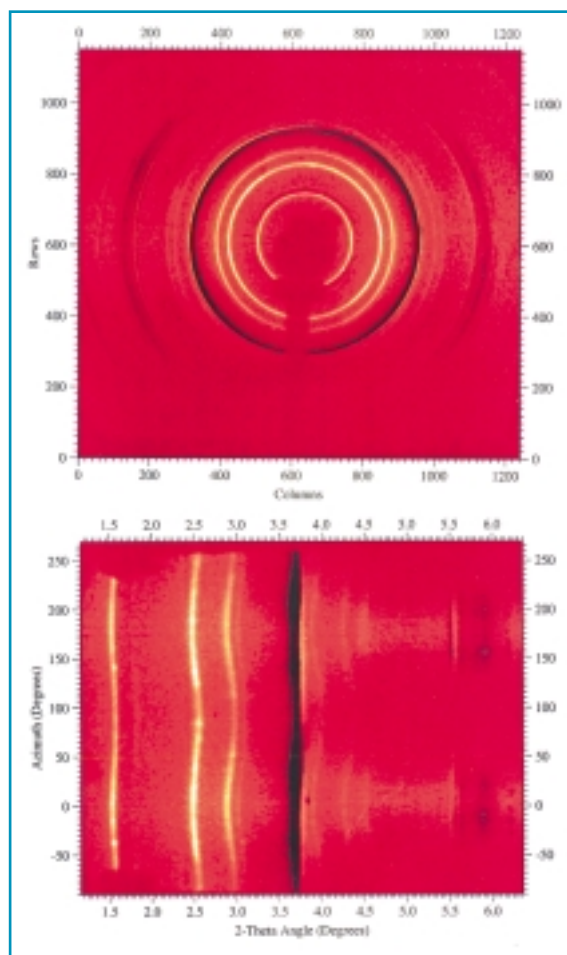
Fig. 4: In situ diffraction image and the corresponding unrolled projection along an azimuthal angle. The pressure and temperature of the experiment were P = 2 GPa and T = 473 K.

VACANCIES AT THE ESRF ON 14 SEPTEMBER 1999

	Ref	Subject	Deadline
SCIENTIST	2184	for the High Energy beamline ID15A	30/09/99
	2119	For the Magnetic Scattering Beamline ID20	30/09/99
Previous post-doctoral experience with synchrotron radiation is essential.			
POST-DOC	PDBM14	Two Post-docs for Macromolecular Crystallography beamlines	30/09/99
	PDID30	For the Large Volume Cell Program at the Beamline ID30	05/11/99
	PDID30-2	For the Laser Heating Program at the Beamline ID30	05/11/99
ENGINEERS	2214	Three Computer Engineers - *corrected version*	15/10/99
	5125/5126	Two System Administration Engineers	05/11/99
TECHNICIANS	1513	Radiation Protection Technician	08/10/99
	4524	Power Supply Technician	15/10/99
	2550	Technician in Chemistry	31/10/99
	2536	Technician in Electronics	15/11/99

If you are interested, please send us a fax (+33 (0) 4 76 88 24 60) or an e-mail (recruitm@esrf.fr) with your address, and we will provide you with an application form. You can also print out an application form on the World Wide Web http://www.esrf.fr

Time-resolved SAXS Study of Conformational Changes in the Chaperonin System GroE

M. Roessle[1], E. Manakova[1], I. Lauer[2], T. Nawroth[2], R. Gebhardt[2], T. Narayanan[3] and H. Heumann[1]

1 Max-Planck-Institut fuer Biochemie, Martinsried (Germany)
2 Biochemisches Insitut der Universitaet Mainz, Mainz (Germany)
3 ESRF, Experiments Division

Time-resolved small-angle solution scattering was performed on the chaperonin system GroE from E. coli in order to obtain structural and kinetic data along the reaction pathway of a chaperonin system. This investigation was made possible owing to the high brilliance of a third generation synchrotron source and the development of fast 2-D detectors, permitting real-time small-angle scattering measurements in the millisecond regime even on weakly scattering samples.

The biological functions of proteins are directly connected to the dynamics and the conformational changes within the domains of protein as well as the association-dissociation processes between interacting proteins. Many of these processes occur only in the aqueous physiological environment. Conformational changes of proteins in the millisecond to second time range can be followed by relatively low resolution methods, such as time-resolved small-angle x-ray scattering (TRSAXS), by exploiting the high flux available at a synchrotron source like the ESRF. The application of this method requires rapid mixing of the components as well as fast image acquisition. By using a stopped-flow device for fast mixing (mixing time < 20 ms), we have investigated the chaperonin system GroE from E. coli. Molecular chaperonins are helper proteins which are essential for living cells to repair incorrectly folded polypeptides, such as denatured proteins. The chaperonin system GroE consists of the main chaperonin GroEL (800 kDa) and the co-chaperonin GroES (70 kDa), which are proteins that assist the refolding of unfolded proteins [1]. GroES, a heptameric ring, binds during the reaction cycle to one end of the 14meric GroEL hollow cylinder [1,2]. The dissociation of GroES as well as the re-folding process are facilitated by the ATPase activity of GroEL [2], whereby ATP is hydrolyzed to ADP (Figure 1).

The stopped-flow device schematically shown in Figure 2 consists of two syringes driven by a remote-controlled stepping-motor system and a fast mixer. The data acquisition is triggered by the signal from this device which becomes active once the injection of the two syringes is completed. The protein denaturation due to radiation damage (~ 2 x 10^{13} ph/s/mm^2 at 12.5 keV) and
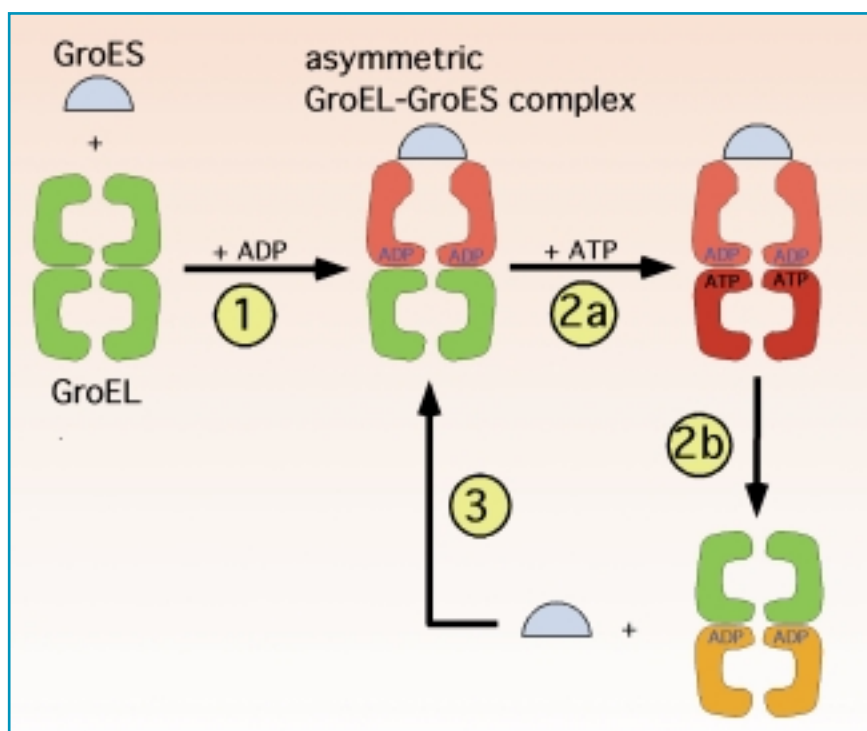

Fig. 1:
Reaction cycle of the GroE system without denatured substrate protein. The asymmetric GroEL-GroES complex shows a high affinity for substrate protein and is therefore an important starting structure in the re-folding cycle.

Fig. 2:
Schematic of the stopped flow device used for the time-resolved small-angle x-ray scattering. The full details of the sample environment box are not shown.
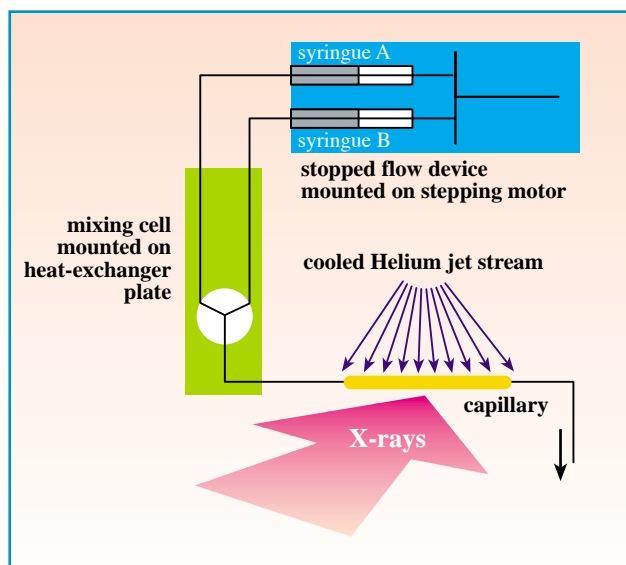
beam heating were avoided by using glycerol as a radical quencher and a jet stream of cooled He-gas directed on to the sample capillary at the beam position. Despite these precautions, radiation damage could not be fully eliminated for long exposures (> 30 s). 2-D SAXS patterns were acquired using the fast XRII-FRELON CCD detector system. This detector system is capable of acquiring 10 images per second with a resolution of 1024x1024 pixels with a dynamic range of 14 bit. By adjusting the typical exposure time (150 – 200 ms) required for these samples which scatter weakly, it was possible to take about 110 time slices within a total acquisition time of 33s.

As a starting point, we have investigated the binding kinetics of GroES to GroEL in the presence of ADP - the first step in the chaperon cycle shown in Figure 1. In this experiment, GroEL (syringe A) and GroES together with ADP (syringe B) were mixed together. The subsequent steps of the chaperonin cycle, steps 2a to 3 in Figure 1, have been analyzed in a second experiment where the pre-formed GroEL-GroES complex (syringe A) was mixed with ATP (syringe B). The radius of gyration (R_g), which provides sensitive information about the shape of the particles (deduced from the measured scattering curve), was used to follow the reaction. Reference measurements of the proteins mixed with buffer solutions containing no nucleotides were also performed.

The resulting data are shown in Figures 3a and 3b. The increase of the R_g-values in Figure 3a indicates the formation of the asymmetric GroEL-GroES complex. The reaction was finished within about 8 s after mixing. The time evolution of R_g- values in the second experiment, which probed the change of the pre-formed GroEL-GroES complex after mixing with ATP (Figure 3b), revealed an unexpected
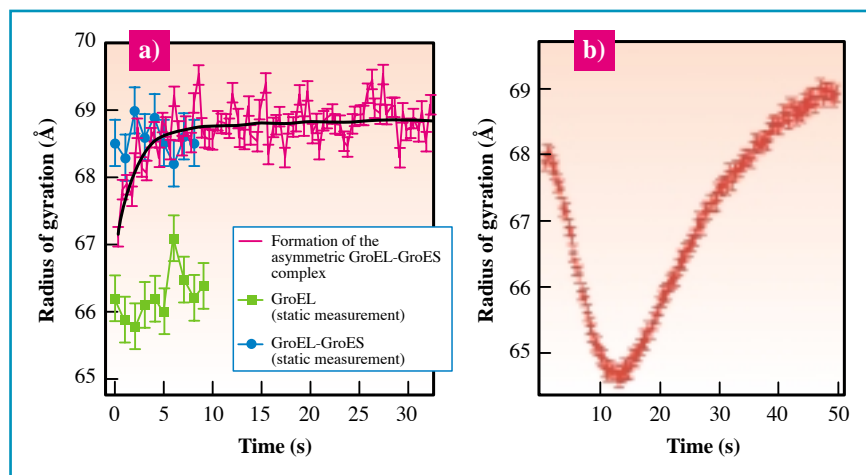

Fig. 3:
Results of the real-time analysis along the reaction pathways of the chaperonin system GroE:
a) Association of the GroEL and the GroES in the presence of ADP.
b) The reaction of the GroEL and GroES in the presence of ATP.

behavior. The measured radius of gyration immediately after mixing decreases and reaches a minimum after 13 s. Then, the value increases again for about 40 s. This variation suggests that the binding and hydrolysis of ATP, mediated by the GroE-associated ATPase is a multi-step process. The decrease of the R_g-value can be attributed to the dissociation of GroEL and GroES upon ATP binding and hydrolysis. After about 13 s, the dissociation process is completed and the second step begins, which is the rebinding of the GroES, is started.

In conclusion, our results indicate that the interaction between GroEL and GroES is a multi-step process in the presence of ATP while it is a fast single-step process in the presence of ADP. ■

REFERENCES
[1] Z. Xu, A.L. Horwich, P.B. Sigler, Nature, 388, 741-750 (1997).
[2] H.S. Rye, A.M. Roseman, S. Chen, K. Furtak, W.A. Fenton, H.R. Saibil, A.L. Horwich, Cell, 97, 325-338 (1999).
[3] R. Stegmann, E. Manakova, M. Roessle, S. Nieba-Axmann, T. Hermann, R.P. May, A. Wiedenmann, A. Plueckthun, H. Heumann, Journal of Structural Biology, 121, 30-40 (1998).

Fiber Diffraction and Small-Angle Scattering on Single Cellulose Fibers

M. Müller, M. Burghammer and C. Riekel

ESRF, Experiments Division

Microdiffraction experiments at the ESRF Microfocus beamline (ID13) on single cellulose fibers have already been reported in 1995 [1]. Since then, a considerable amount of fiber diffraction experiments has been performed and the experimental setup has been further developed. The present article will show some of the most recent experimental results on cellulose.

Cellulose fibers, both native and artificially produced, play a major role in daily life. They are present in textile fabrics (cotton, linen, viscose), paper and construction materials (wood). Detailed structural information down to the level of a single fiber are needed in order to understand and to optimize the unique mechanical properties of these materials.

At ID13, monochromatic beams of 10 μm and 2 μm in diameter (produced presently by an ellipsoidal mirror and subsequent beam definition by collimator or glass capillary [1], respectively) are used for position-resolved diffraction and – more recently – for small-angle scattering experiments [2]. Ideally, information on three different length scales is obtained simultaneously [3]:

(i) The sample is scanned on the micrometer scale, corresponding to optical microscopy.

(ii) Wide-angle diffraction contains information on crystallographic parameters such as cell constants or orientation.

(iii) Small-angle scattering is sensitive to inhomogeneities on intermediate length scales (here, typically 1 nm to 10 nm).

The so-called « scanning set-up » on ID13 is, therefore, particularly suitable for the investigation of hierarchically structured materials like cellulose.

Cellulose molecules aggregate forming small crystals called *microfibrils* (a few nm in diameter). The morphology of native and artificial cellulose fibers, i.e. the arrangement of the microfibrils, is of great variability. Many fibers are further structured on a microscopic scale. In the following, three examples will be given to demonstrate how the x-ray microbeam is used in order to obtain information on the different hierarchical levels of cellulose organisation.

The investigation of a *single viscose rayon fiber* (F295, Fibro®, Courtaulds Research and Technology) demonstrates the advantage of the x-ray method with respect to selected area electron diffraction [4]. A single fiber is used in the experiment, and no tedious and time-consuming sample preparation like embedding and sectioning is necessary. In addition, more quantitative diffraction diagrams can be obtained due to the weaker interaction of x-rays with matter (i.e. less beam damage and no multiple scattering).

MICROSTRUCTURE SEEN BY ELECTRON MICROSCOPY

The fiber, having a diameter of 9 μm, was scanned with a 2 μm beam in steps of 2 μm. Figure 1 shows a scanning electron microscopic image of the fiber with a characteristically serrated surface. The two circles signify the areas illuminated by x-rays in the center of the fiber and at its edge, respectively. Below each circle, the respective fiber diffraction diagrams (cellulose II structure, see also [1]) are found as insets. There is a clear indication of a « skin-core » microstructure for this viscose fiber: The orientation of the cellulose microfibrils at the fiber edge is better, resulting in better defined Bragg reflections in the diffraction diagram. From transmission electron micrographs, there is evidence for a 2 μm thick skin layer [4]. Using this number, the core/skin volume ratio for the skin + core pattern (Figure 1) can be estimated. A « pure core » diffraction
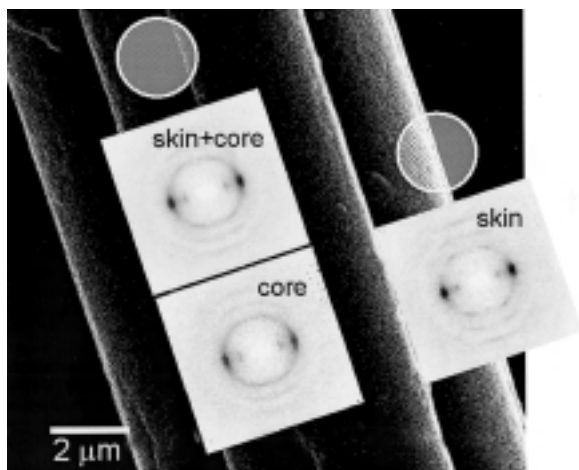

Fig. 1: Skin-core microstructure of a viscose rayon fiber (diameter 9 μm). In the skin layer with a thickness of about 2 μm the cellulose crystals are far better oriented than in the fiber core, resulting in sharper diffraction spots in the fiber diffraction diagram. (Wavelength 0.782 nm, 2 μm beam, image-intensifier CCD detector, 96 s exposure.).

Fig. 2: Scattering curve of a single native flax fiber on a double-logarithmic scale (azimuthal integration of the two-dimensional scattering pattern; wavelength 0.96 nm, 10 μm beam, CCD detector, 240 s exposure). Data in the small-angle region (SAXS) as well as high-order Bragg reflections (WAXS region) were obtained simultaneously on a single detector.
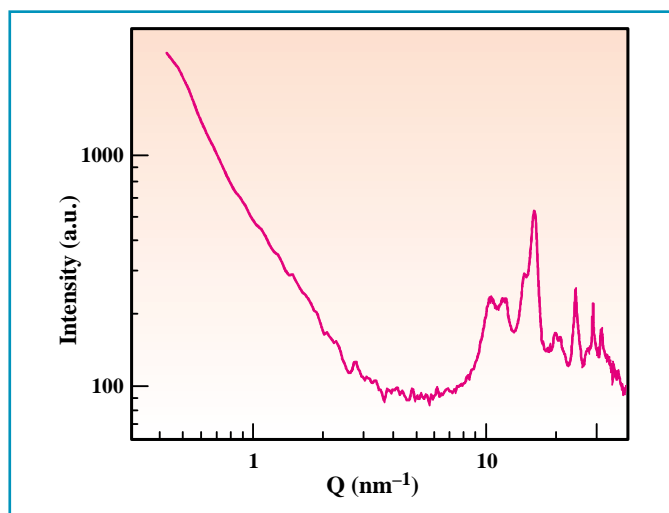
diagram (Figure 1) is then obtained by taking the difference of the centre and the edge patterns with the appropriate scaling. It can now clearly be seen that the orientation of the cellulose microfibrils inside the fibre core is much worse (by a factor of two) than in the skin layer. Note that a quantitative fiber diagram has already been obtained from a very small volume of cellulose (of the order of 10 μm^3 for the pattern at the fiber edge).

MICRODIFFRACTION

The main interest in *single flax fibers* (average diameter 20 μm) concerns the disorder present in all native cellulose specimens, both inside the microfibrils and in their arrangement in the fiber. It is, therefore, necessary to extend the microdiffraction experiments into the SAXS-range. It has recently been shown that both a fiber diagram and a small-angle scattering pattern can be simultaneously recorded on a single CCD detector with a 10 μm beam [3]. The scattering curve, resulting from azimuthal integration, is shown in Figure 2. A range of d-spacings from 15 nm to 0.21 nm is covered. The small- and wide-angle regions are not clearly separated, but connected by a continuous streak of intensity, which is in fact concentrated on the equator of the diagram (see also Figure 3). This scattered intensity is – together with a diffuse maximum below the Bragg reflections at Q ~ 15 nm^{-1} – probably due to disordered cellulose molecules between the ordered (crystalline) microfibrils. As most of these molecules are located on the surfaces of the microfibrils, they retain their alignment with the fiber axis. This one-dimensional order gives rise to the orientation of the corresponding scattering pattern.

A second experiment on flax explored the present limits of the signal-to-noise ratio in single fiber diffraction [3]. A small beam stop (400 μm in diameter) was moved very close (5 mm)

Fig. 3: Fiber diffraction pattern of a single flax fiber at 100 K (wavelength 0.782 nm, 10 μm beam, CCD detector, 120 s exposure). The fiber axis was oriented nearly horizontally and corresponds to the meridian of the diffraction diagram; the equator is perpendicular to the fiber axis. The resolution limit is d = 0.113 nm (009 reflection on the meridian).
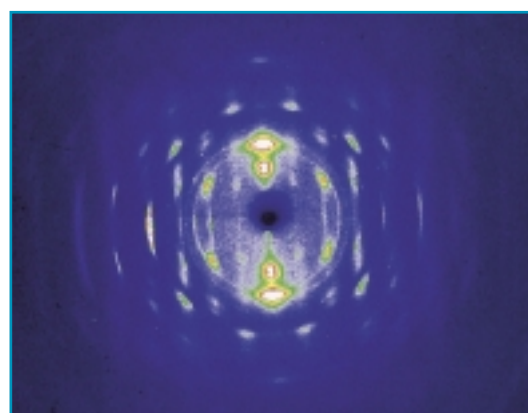
to the sample in order to keep the air scattering background signal at a minimum. Using a liquid nitrogen cryostream, the fiber was cooled to 100 K. The low temperature reduces thermal vibrations of the atoms in cellulose and, thus, enhances the intensity of high-order Bragg reflections. Figure 3 shows the measured fiber diagram. In the meridional direction, the 009 reflection (d = 0.113 nm) is observable, whereas along the equator the 600 (d = 0.131 nm) is the highest indexed reflection. These observed smallest d-spacings correspond to the diffraction limit of the cellulose crystals. The excellent signal-to-noise ratio enables furthermore the observation of diffuse scattering along the layer lines of the diffraction diagram. This diffuse intensity is an indication of defects inside the microfibrils, which are probably related to cellulose biosynthesis. A quantitative analysis of these very recent data is under way.

Cellulose is just one example of hierarchically structured biopolymers. The method described here can be equally well applied to a large field of problems in biopolymer science.

Studies on wood, chitin, starch, spider silk and collagen are current topics of research at the Microfocus beamline. Of particular interest for future microdiffraction studies using beams in the micrometer and sub-micrometer range is the breakdown of fiber symmetry which has already been observed for certain of these systems, chitin [5] being one example. ∎

REFERENCES

*[1] P. Engström, C. Riekel, H. Chanzy, ESRF Newsletter **24**, 8-9 (1995).*

*[2] C. Riekel, P. Engström and C. Martin, Journal of Macromolecular Science - Physics **B37**(4), 587-599 (1998).*

[3] M. Müller, C. Czihak, M. Burghammer, C. Riekel, J. Appl. Cryst., submitted.

[4] M. Müller, C. Riekel, R. Vuong, H. Chanzy, Polymer, in press.

[5] M. Burghammer, H. Chanzy et al., unpublished.

STRUCTURE OF THE NUCLEAR TRANSPORT RECEPTOR IMPORTIN β BOUND TO THE IBB DOMAIN OF IMPORTIN α

G. CINGOLANI, C. PETOSA AND C. W. MÜLLER

EMBL, GRENOBLE OUTSTATION (FRANCE)

Not only does x-ray crystallography provide structures of individual biological macromolecules, but also it can show in detail how these molecules act in concert to fulfill specific functions in a living cell. Using beamlines at the ESRF the atomic structure of a nuclear transport receptor complex has recently been determined [1]. The complex structure leads to a deeper understanding of how molecules are transported in and out of the cell nucleus.

A defining feature of eukaryotic cells is the separation between the cell nucleus, where genetic information is stored and where transcription of DNA into RNA occurs, and the surrounding cytosol where messenger RNA molecules are translated into proteins. This spatial separation requires intensive traffic between the nucleus and the cytosol but also offers many possibilities for regulation. Exchange between the two cellular compartments occurs through the nuclear pore complex (NPC), a ~ 125 MDa structure containing approximately 100 different polypeptides embedded in the nuclear envelope. The nuclear pores allow passage by passive diffusion of molecules up to 40 kDa, but most molecules are actively transported bound to nuclear receptors [2].
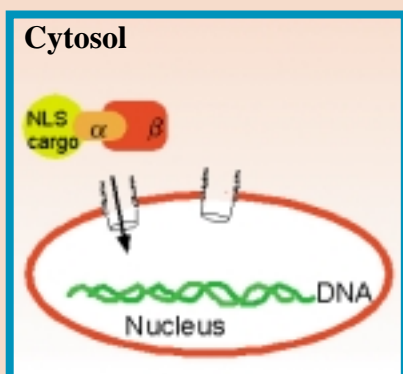
Targeting of many proteins to the nucleus is determined by the presence of a nuclear localization sequence (NLS), a short sequence containing one or two clusters of basic amino acid residues. An NLS-bearing substrate, often termed the "cargo", is delivered to the nucleus by association with the heterodimer formed by importin α and importin β (also called karyopherin-α and -β). Importin α recognizes the NLS while importin β is responsible for docking to the NPC and translocation through the pore (Figure 1). Dissociation of the NLS-cargo:importin α:importin β trimer is triggered by the association of importin β with the protein Ran, a Ras-related GTPase. In the nucleus Ran is predominantly bound to GTP (a small molecule related to the cellular energy carrier ATP) while in the cytoplasm it is bound to its lower-energy analogue GDP. This uneven distribution leads to the correct spatial coordination of cargo release because importin β is recognized by RanGTP but not by RanGDP.

GLOSSARY

Eukaryotic cells: contain a cell nucleus and organelles. A eukaryotic cell can be a single cell organism or a part of a multicellular organism such as man.

Cell nucleus: contains the genetic information of the cell which is stored as a long linear DNA molecule. The nucleus is surrounded by a membrane, the nuclear envelope.
In the nucleus, DNA is constantly transcribed into RNA molecules which are exported to the cytosol.

Proteins: are chains of amino acid residues, which usually adopt well defined structures. Proteins are made in the cytosol where a cellular machine, the ribosome, translates messenger-RNA into proteins.

Nuclear pore complex (NPC): are large pores embedded in the nuclear envelope which allow the passage of proteins and RNA molecules between the nucleus and the cytosol.

Nuclear localization sequence (NLS): are short peptide sequences which serve to direct proteins containing them into the nucleus.

Importin α, β: are nuclear transport receptor molecules. Proteins containing NLS bind to importin α, which in turn interacts via its N-terminal importin ß-binding (IBB) domain with importin ß. The trimeric import complex is translocated through the nuclear pore.

Ran: is a small GTP-hydrolyzing enzyme. It is found in a complex with GTP, the higher energy form of triphosphate nucleotide, in the nucleus and in a complex with GDP in the cytosol. In the nucleus, binding of RAN to GTP leads to the dissociation of the trimeric import complex.

HEAT motifs: are sequence repeats found in several eukaryotic proteins. X-ray structures show that HEAT motifs consist of two α-helices, A and B, which are connected by a short turn.

Fig. 1: Schematic representation of the import cycle. NLS-containing cargo molecules are bound via the adapter molecule importin α to importin β. Following transport through the nuclear pore, binding of RanGTP to importin β dissociates the trimeric complexes. Importin β / RanGTP leaves the nucleus and dissociates in the cytosol after hydrolysis of RanGTP to RanGDP.

Importin α is a 60 kDa protein composed of a small N-terminal domain and a large NLS-binding domain connected by a flexible linker. The NLS-binding domain of importin α forms an elongated right-handed superhelix with a shallow groove where the NLS peptide is bound. The N-terminal domain, termed importin β binding (IBB) domain, is a basic stretch of approximately 40 highly conserved residues which are minimally required for binding importin β and for efficient nuclear entry. The IBB domain is thus the nuclear targeting signal of importin α.

Importin β is a 97 kDa protein and is the best characterized member of a superfamily of homologous nuclear transport receptors. Members of this superfamily vary between 90 and 130 kDa in size and are characterized by an N-terminal Ran-binding region and by NPC-binding activity. Sequence comparisons predicted importin β to contain a number of tandem HEAT motifs, sequence repeats of roughly 40 residues found in a variety of eukaryotic proteins. Apart from the classical protein import pathway, importin β is also involved in the nuclear import of ribosomal, cell-cycle-controlling and viral proteins (including HIV-I proteins), which bind directly to importin β without using the adapter molecule importin α.
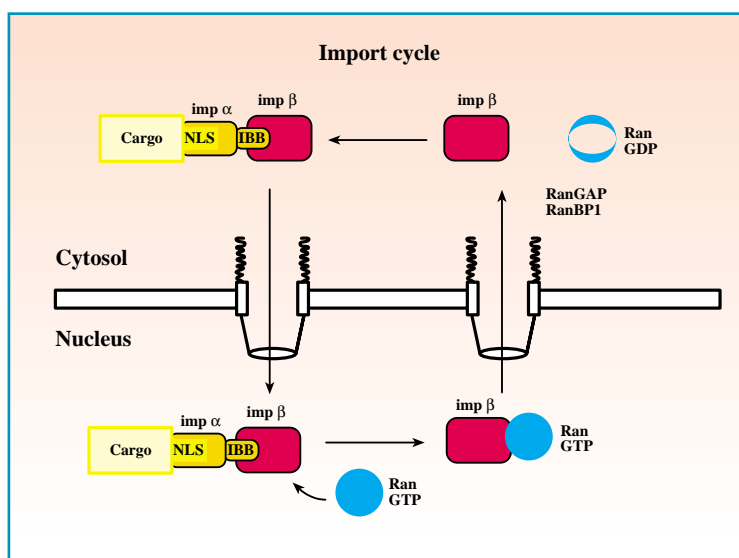
STRUCTURE DETERMINATION

Co-crystallization experiments of importin β overproduced in bacteria together with a chemically synthesized IBB-domain peptide gave rise to crystals which diffracted beyond 2.5 Å resolution. Native data sets were collected from two crystal forms at beamlines ID14-3 and ID2 to 2.5 Å and 2.3 Å resolution, respectively. Solving the structure by conventional heavy-atom soaks turned out to be difficult because of significant non-isomorphism between native and derivative crystals. Therefore selenomethionine substituted importin β was produced, and the structure of the complex was solved by the multiwavelength anomalous diffraction (MAD) method at the "MAD-beamline" BM14 of the ESRF. This powerful technique, which uses the signal of anomalous scatterers in the crystal, is nowadays routinely used to solve the "phase problem". Its application is further facilitated through the automated "MAD and MIR structure solution" program SOLVE, which in our case successfully located 21 out of the possible 24 selenium atoms. 38 polyalanine helices were placed into the first experimental electron density at 3.3 Å resolution. Recombination of MAD phases with those calculated from the model yielded a map allowing much of the sequence to be traced. The chain tracing of importin β was greatly expedited by the selenium peaks in an anomalous difference Fourier map. The final refined model at 2.5 Å resolution has an $R_{cryst} = 22.1\%$ and $R_{free} = 27.3\%$, and consists of IBB domain residues α11- α54, all 876 importin β residues, and 44 water molecules.

OVERVIEW OF THE COMPLEX

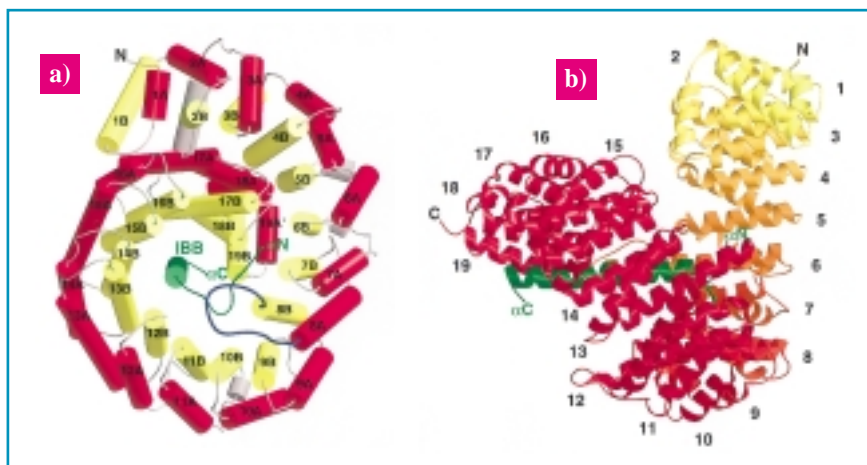The structure of the complex is shown in Figure 2. The complex takes

Fig. 2: Structure of importin β bound to the IBB domain of importin α. a) View down the superhelical axis. A and B helices are shown in red and yellow, respectively with connecting residues in grey. The loop in HEAT repeat 8 containing mostly acidic residues is depicted in blue, the IBB domain in green. b) orthogonal view with respect to a. The ribbon representing importin β is colored progressively from yellow to red as the chain proceeds from N- to C-terminus.
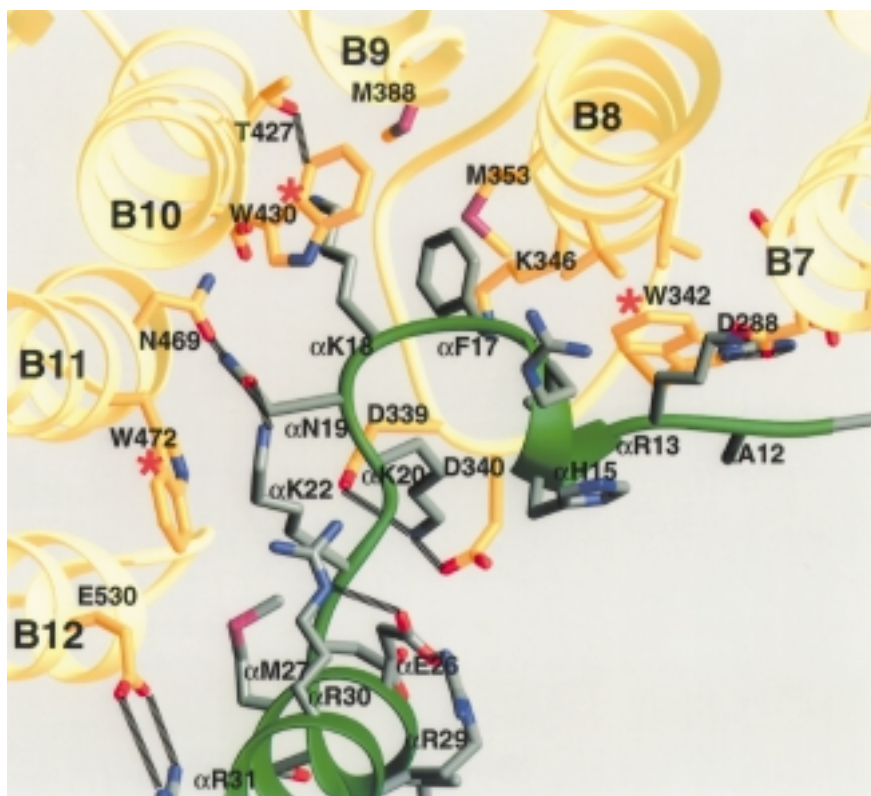
on a snail-shaped appearance with the IBB domain at the center and importin β wrapped around the outside. The complex adopts a highly compact, essentially globular shape with a diameter of 85 Å. Importin β is an all helical protein composed of 19 tandem HEAT repeats, arranged in a right-handed superhelix with a pitch and mean diameter both equal to approximately 50 Å. The relatively short pitch results in N- and C-terminal HEAT repeats nearly touching each other, giving the molecule a rather "closed" appearance. Each HEAT repeat is composed of an A and a B helix connected by a short turn of residues and varies between 32 and 61 residues in size. Repeats are arranged within the molecule so as to yield an outer layer of A helices defining the convex surface, and an inner layer of B helices defining the concave surface. Repeats 7 to 19 are responsible for the recognition of the IBB domain, while HEAT repeats 1 to 6 are not involved in the IBB binding but interact with RanGTP.

The IBB domain is intimately bound on the inner surface of importin β and adopts an L-shaped conformation. An N-terminal moiety (residues α11- α23)

and a C-terminal helix (residues α24-α51) run in mutually perpendicular directions, with the C-terminal helix roughly coinciding with the importin β superhelix. Basic residues account for nearly 40% of the IBB domain, creating an electrostatic surface potential complementary to that of the inner surface of importin β, which is lined with acidic residues. The intermolecular interactions are intimate, involving 42% of the surface area of the IBB domain. Nearly every residue in the IBB N-terminal moiety interacts with a B helix in HEAT repeats 7 to 11 and with one prominent loop containing mostly acidic residues in HEAT repeat 8 (Figure 3), while the IBB helix packs against helices from HEAT repeats 12 to 19.

CONFORMATIONAL CHANGES OF TRANSPORT RECEPTORS

The closed conformation of importin β and the eight-HEAT "embrace" of the IBB helix suggests that a significant conformational change may occur upon binding or release of

the IBB domain. Probably importin β adopts a more open conformation when not bound to the IBB domain of importin α. This is corroborated by the structure of a homologous transport receptor (transportin or karyopherin β-2) bound to Ran:GppNHp which was published at the same time as our complex [3]. In that structure the cargo has been released upon the binding of Ran:GTP and the C-terminal part of transportin adopts a much more open conformation than in the importin β:IBB domain complex. While these two complementary complex structures do not reveal everything we wanted to know about nuclear transport, they nevertheless provide a good starting point for asking even better questions. ■

REFERENCES

[1] G. Cingolani, C. Petosa, K. Weis, C.W. Müller, Structure of importin-β bound to the IBB domain of importin-α, Nature, 399, 221-229 (1999).

[2] I.W. Mattaj, L. Englmeier, Nucleocytoplasmic transport: the soluble phase, Annu. Rev. Biochem., 67, 265-306 (1998).

[3] Y.M. Chook, G. Blobel, Structure of the nuclear transport complex karyopherin-β2 Ran:GppNHp, Nature, 399, 230-237 (1999).

How do the Dislocations Multiply at the Onset of Plastic Deformation in Silicon ?

F. Vallino[1], A. Jacques[1], A. George[1], J. Baruchel[2] and M. Schlenker[3]

1 Laboratoire de Physique des Matériaux, CNRS-INPL-UHP Nancy 1, Nancy (France)
2 ESRF, Experiments Division
3 Laboratoire Louis Néel, CNRS, Grenoble (France)

In situ x-ray topography of initially defect-free silicon crystals submitted to tensile stress at elevated temperature has provided evidence that dislocation arrays become non-planar with time, that cross-slip events are frequent even in the bulk and that sources of primary slip dislocations can be formed with the help of secondary slip systems.

P lastic deformation, the part that remains after stress has been removed (as opposed to elastic deformation), is tremendously important because it is used to shape many of the objects around us - car bodies for example. It is now well known that plastic deformation is related, at the microscopic level, to the behavior of line-shaped crystal defects, known as dislocations. However, a lot remains to be learned about the physics of this process. The present investigation deals with silicon, a fascinating material in many ways. On the one hand, silicon is grown industrially, for the microelectronics industry, in the form of single crystals with unprecedented purity, or with small, perfectly controlled, amounts of impurities (this process of doping is essential in electronics). This is convenient for the investigation of dislocation movement because impurities interact with dislocation lines. On the other hand, plastic deformation of silicon at room temperature does not occur - another unusual property of silicon, making it valuable in micro-mechanical applications such as ink-jet nozzles. Furthermore, silicon crystals are usually dislocation-free in the as-grown state, and achieving plastic deformation (at high temperatures) implies that dislocations have to be created and have to multiply. Finding out how this occurs, through direct observation, is the purpose of the present work.

HOW DO DISLOCATIONS MULTIPLY ?

In crystals, plastic deformation generally proceeds by a glide of dislocations (see insert). Therefore, initially dislocation-free materials, like silicon, raise a simple question: how do dislocations multiply during the first stages of plastic deformation until they reach a typical density of about 10^8 cm.cm^{-3} at the macroscopic yield point?

When a dislocation-free silicon sample is submitted to an applied stress at a temperature high enough for dislocations to be mobile, the first dislocations form at residual defects acting as stress concentrators, preferentially surface defects resulting from machining (scratches, micro-cracks...), more rarely internal micro-defects inherited from crystal growth. However, such defects are too few to account for the observed filling of the whole sample with dislocations. Therefore, new sources must be continuously generated during plastic deformation, and most probably these new sources are formed by the existing dislocations themselves.

The basic configuration for dislocation multiplication is the Frank-Read source (see text in the frame) consisting of a dislocation segment which bows out between two pinning points, generating a set of concentric

<div style="border:1px solid">

GLOSSARY

Dislocation: It is a line defect characterized by its direction **l**, which changes if the dislocation is not straight, and its **Burgers vector b**, which is constant along the whole dislocation. **b** defines the shear displacement produced in the crystal when the dislocation crosses it.
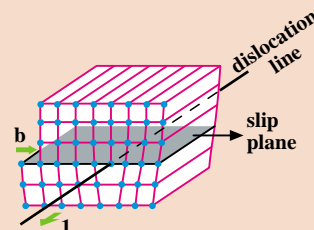
Frank-Read source: A dislocation segment, pinned at its extremities, (a), bows out in its slip plane under the shear stress (b, c). The two opposite dislocation segments annihilate, generating a closed loop and restoring the initial configuration (c, d).
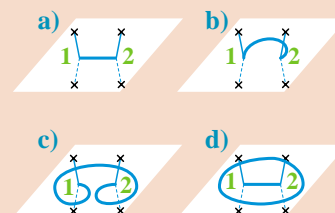
Schmid factor: The stress which does work when a dislocation glides is the shear stress parallel to the slip plane, in the direction of the Burgers vector. The relationship between the resolved shear stress τ, on a given slip system, and the applied tensile stress σ, is $\tau = s.\sigma$ where s is the Schmid factor $s = \cos \varphi \cos \nu$ $(0 \leq s \leq 0.5)$.

</div>
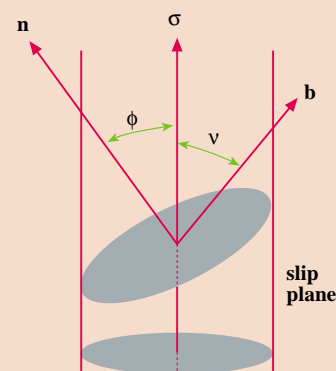
loops. The multiplying segment must have first escaped from its original slip plane and have been transferred onto a parallel plane, where it is free to bow out around pinning points. In fcc crystals, this is usually assumed to proceed by double cross-slip, since dislocations with 1/2<110> Burgers vector can glide in two dense {111} planes. However, cross-slip is not a simple process and conditions for its occurrence are still poorly known, especially in the bulk. The purpose of the present experiment was to shed some light on this mechanism.

The understanding of the rather complex behavior of dislocations has largely relied on their observation, and continues to do so. Because they entail long-range distortion of the lattice, dislocations can locally affect Bragg diffraction, hence be seen through transmission electron microscopy (TEM) in thin foils, and, in the bulk, by x-ray Bragg-diffraction imaging, traditionally called x-ray topography. An important feature is that both characteristics of single dislocations can be assessed, in particular through the disappearance of the image ("out-of-contrast" situation) for some Bragg reflections.

WHY TOPOGRAPHY ?

Dislocation sources were observed by *in situ* TEM but, in thin foils, surface effects are predominant. X-ray topography offers a unique possibility to observe large volumes of crystal, under well-defined stress and temperature

conditions. Its main drawback is a spatial resolution which limits the acceptable dislocation density to $\sim 10^4$ cm.cm^3, far below its value at the macroscopic yield point. The present study was based on synchrotron radiation Bragg-diffraction imaging, which is very well suited to *in situ* investigations, at the ESRF ID19 beamline. It was complemented by the laboratory technique for x-ray topography, Lang's method.

In silicon, dislocation velocity is thermally activated and is roughly proportional to the resolved shear stress τ, which, on a particular slip system is equal to s • σ, where s is the Schmid factor (see insert) and σ the applied stress. The kinetics that are compatible with *in situ* observations at the ESRF prevail at temperatures of $\sim$ 1000 K under nominal stresses σ of about 25 to 50 MPa, which are convenient for tensile testing.

Experiments were performed with a mechanical testing system custom designed and constructed at Nancy for the "horizontal" diffractometer of the ID19 beamline. Tensile samples ($\sim$ 15 x 4 x 0.7 mm^3 in size) were used. The stress axis was parallel to [1, $\bar{1}$, 4], which corresponds to a double slip orientation, with two primary slip systems of s $\sim$ 0.45. Corresponding cross-slip systems had s $\sim$ 0.23. The samples were polished with great care, in order to remove machining defects. Vickers micro-indentations were made on the large faces of the samples in order to nucleate the first dislocations.

Dislocation configurations were followed under creep conditions

(constant stress and temperature), in a neutral gas to avoid oxidation. Topographs were recorded on x-ray films, using a –2,2,0 Bragg reflection with a monochromatized beam ($\lambda \sim$ 0.7 Å) at chosen time intervals. The FRELON camera was used for real-time observations of the evolving configurations. The experiments were stopped before the dislocation density was too high, so that a complementary stereo-pair and Burgers vector analysis could be performed later by conventional Lang topography. Since plastic deformation always created elastic strain gradients in the sample, it was necessary to scan over $\sim$ 0.02 - 0.1 degrees around the Bragg angle to obtain a full image, so that the exposure time could not be less than 30 seconds.

ANALYSIS OF THE TOPOGRAPHS

Figure 1 shows two topographs from a sequence recorded at T = 1070 K, σ = 22 MPa and a Lang topograph of the final configuration. A dislocation source, labeled S, can clearly been seen. Such a source was seldom observed and it results from a complex sequence. What follows is a description of some of the elementary mechanisms involved:

(i) cross-slip. Its presence is apparent from the hexagonal half- or full-loops (marked by arrows on Figure 1c) coming out of dense slip bands. These bands consist of 1/2 [$\bar{1}$,0,1] dislocations lying in (1,$\bar{1}$,1) planes, which are seen nearly end-on here. Analysis confirmed that out-going loops have the same Burgers vector and develop in (111), i.e. the corresponding cross-slip plane. Further, cross-slip started in the bulk and not at a free surface.

(ii) non-planarity of dislocation arrays. Another striking feature appears on the dislocation array running from right to left above the source. Only

Fig. 1: Evolution of dislocation configurations in silicon:
a,b) -2,2,0 in situ topographs at T = 1070 K, σ = 22 MPa.
c) 1, $\bar{1}$, $\bar{1}$ Lang topograph, Mo Kα radiation.
a) t = 14 min. b) t = 19 min. c) after cooling down at t = 27 min, no stress applied.
S: dislocation source; arrows in (c): cross-slipped loops.
X: 3 dimensional configuration formed on two intersecting {111} planes (see text).
Marker: 1 mm;
The applied tension is vertical. The direction of the diffraction vector used for each topograph is indicated by its projection on the image plane.

one slip system is active in this band, which is out-of-contrast in Figure 1c, topograph: 1/2 [0,$\bar{1}$,1](111) (s ~ 0.454). As usual in silicon, the leading dislocations (seen on the left) are straight and parallel to [0,$\bar{1}$,1]. Dislocations become more and more wavy as their distance from the leading ones increases. They then consist of segments developing in several parallel planes connected by jogs. Such non planar configurations may result from cross-slip, but also from climb due to absorption or emission of point defects. Jogs may provide pinning points for a Frank-Read source.

(iii) reactions with secondary slip systems. Unexpected dislocations with low s were repeatedly observed. They were formed at micro-indentations or as the result of reactions between dislocations of other systems. A typical configuration is shown in Figure 1c, where primary dislocations are out-of-contrast. Some dislocations have 1/2 [$\bar{1}$,1,0] Burgers vector and develop simultaneously on (1,1,$\bar{1}$) and (111), both planes having the same resolved shear stress (s ~ 0.18). Such three-dimensional configurations seem to be important for the development of new sources in formerly inactive slip planes.

CONCLUSION

The synchrotron radiation delivered by the ESRF enabled us to perform unique *in situ* observations of evolving dislocations within the whole volume of thick and large crystals under stress. They have revealed several microscopic mechanisms involved in the filling of the samples with dislocations starting from a few initial sources. The temperature and stress dependencies of these mechanisms remain to be determined. This will imply a significant decrease in the exposure times, which should be feasible with the existing equipment through further optimization. ■

Multiplet Structure in High-Resolution Spin-Polarized Fe 2p Photoemission Excited by Circularly Polarized Radiation

C. Bethke, N. Weber, and F.U. Hillebrecht

**Institut für Angewandte Physik, Heinrich-Heine-Universität, Düsseldorf (Germany)**

Magnetic circular dichroism in 2p excitations of Fe was studied by high-resolution spin-resolved core-level photoemission. The highly differential experiment reveals richly-structured spectra which allow the first direct identification of four constituent multiplets in the j = 3/2 final state.

Core-level photoemission spectra of magnetic materials may carry information on the magnetic ground state in two ways: firstly, via the spin polarization of the photoelectrons, and, secondly, by the occurrence of magnetic dichroism. Experimental and theoretical studies addressing these issues for photoemission from the 3d ferromagnets and rare earths have been reported by a number of groups. Electron spin analysis commonly reduces the photoelectron count rate by about three orders of magnitude, which limits spin-resolved experiments to high-performance beamlines at third generation synchrotron sources, such as the ESRF. It is clear that a spin and angle-resolved experiment is the most differential photoemission experiment possible, and therefore may reveal more information on the spectral lineshapes than can be obtained from other experiments. While the photoemission spectra of localized systems, e.g. the rare earths, can be analyzed in a straightforward manner using an atomic approach, systems in which the magnetic moment is carried by delocalized d electrons are far more complicated. For such systems it is not clear to what extent atomic effects prevail, or whether the spectra can be explained within a one electron model. This issue is best addressed in the context of the 2p photoemission spectra of the 3d ferromagnets, because - in contrast to the 3p level which is easily accessible experimentally - the spin orbit splitting is large compared to other interactions, which should simplify the analysis.

For the example of the 2p photoemission lines of the 3d ferromagnets, it is clear from the relatively large line widths observed in conventional photoemission spectroscopy that multiplet interaction must be present in the 2p spectra of 3d ferromagnets [1, 2]: the linewidths are significantly larger than in comparable materials to be attributable only to lifetime broadening. However, to separate the multiplet components experimentally is difficult if not impossible since the splitting between them is comparable to the lifetime broadening. Our goal was to elucidate the detailed spectral features of the 2p photoemission spectrum in a highly differential experiment, combining magnetic dichroism and spin analysis.

As a general rule, magnetic dichroism occurs in photoemission if there is a finite spin polarization caused by spin-orbit interaction along the direction of magnetization. This makes a spin polarized study of magnetic dichroism particularly desirable because, from such a study, one can separate exchange and spin-orbit effects in the photoemission spectra. This was the motivation for our high-resolution study of the Fe 2p level by spin resolved photoemission excited by circularly polarized light. Our results show structures which unambiguously demonstrate the presence of discrete final states in the photoemission spectrum, and allow, for the first time, a direct determination of their energy positions and relative intensities. This

Fig. 1:
Geometry of the experiment and coordinate system with electron wave vector k, magnetization M, and measured component of spin-polarization.
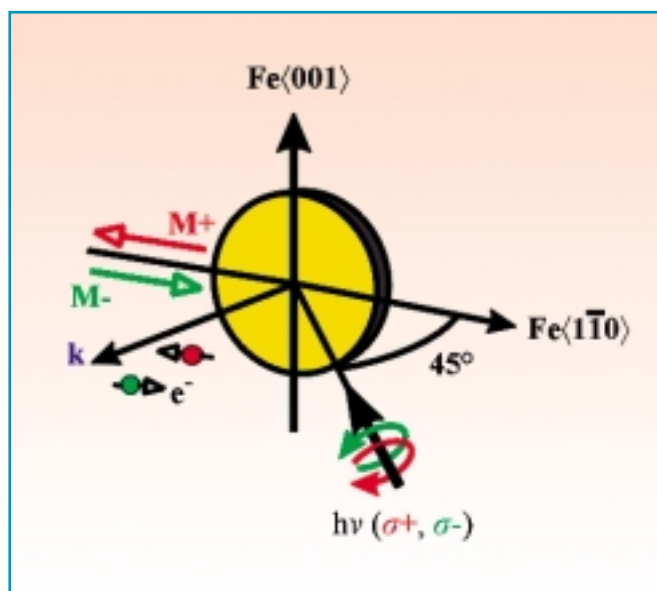
information is vital for an adequate description of core-level photoemission spectra of 3d magnetic systems.

The experiments were carried out at ESRF beamline ID12b, using our photoemission spectrometer equipped with an Fe VLEED spin polarimeter [3]. This method of spin analysis utilizes the spin-dependent reflectivity of a magnetized Fe(100) surface for low energy electrons, which offers a roughly 10 times higher figure of merit than other methods of spin analysis. The samples were grown as ultrathin films (about 20 ML) of Fe on W(110). The overall energy resolution was 0.45 eV. The geometry of the experiment is shown in Figure 1: circularly polarized light from beamline ID12b impinges at 45° onto the sample, and the photoelectrons emitted from the sample are collected in normal emission. The sample is magnetized in the surface plane, in the direction at which the incident light is projected onto the surface. This is also the direction along which the spin polarization is analyzed.

Figure 2 shows spin-resolved Fe $2p_{3/2}$ photoemission spectra excited by 850 eV circularly polarized radiation for fixed light helicity and two opposite sample magnetizations. The background of secondary electrons was subtracted in the usual manner from the spectra. The magnetic dichroism (not shown), i.e. the difference between the two spectra normalized to their sum, amounts to 20%. Since the sample magnetization and the light helicity are at 45°, the observed dichroism extrapolates to an intrinsic dichroism of 28% for this photon energy. In the spin-resolved data, all lineshapes are different, and the individual spectra show characteristic features. To analyze these lineshapes, the spectra were fit with as many Doniach Sunjic lines as required to describe the data. We assume that the spectra are composed of lines with identical binding energies (BE's), with only the intensities changing between the spin channels or with magnetization reversal. The characteristic features in the spectra allow the determination of the number of discrete states present. It is evident from the spectra, that the minimum number of lines to describe the spin-resolved spectra is four: The majority spectrum, Figure 2a, clearly consists of three lines. However, the minority spectrum, Figure 2b, shows a peak at a binding energy lower

Fig. 2: Spin-resolved Fe $2p_{3/2}$ spectrum for magnetization up. Dots show experimental spectrum after background subtraction, lines show fits to the spectra by four Doniach-Sunjic lines. The constituent spectra are shown without applying the experimental broadening of 0.45 eV.
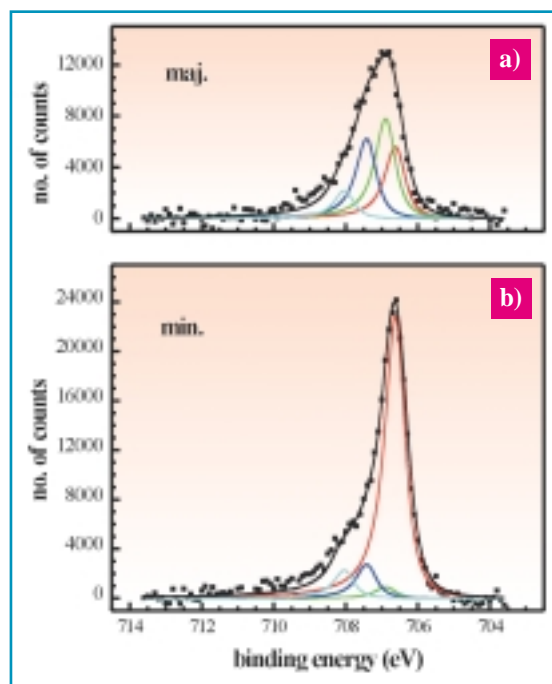
than the lowest binding energy peak evident in the majority spectrum. This can only be described by a fourth line at the appropriate energy. The fits were obtained by an iterative procedure, varying the binding energies of the constituent lines in all spectra (the two spectra shown plus two more for the opposite magnetization) in the same way. The Lorentzian broadening of 0.37 eV, Gaussian broadening of 0.45 eV, representing the experimental resolution, and the asymmetry index $\alpha = 0.2$ were chosen to give an optimum fit to all spectra. The binding energies, relative intensities, and spin polarizations are given in Table 1. The data show that the energy positions of the sublevels are not equidistant. While the splitting between the three higher binding energy lines are 0.62 and 0.53 eV, respectively, the splitting between the two lowest energy lines is only 0.27 eV. This splitting can also be read directly from the spectra in

Figures 2a and 2b.

Overall the fits describe the observed spectra very well. In contrast to previous modeling studies, this analysis is based exclusively on the experimental evidence. Some discrepancies are still present in the region above 708.5 eV binding energy, where the experimental spectra for magnetization down show a tail which is not described by the modeling. The magnetic dichroism curves - also for the linear dichroism - consistently show a broad peak in this energy region. This satellite probably originates from the low spin final states which in the atomic limit are spread out over at least 20 eV. Nevertheless, one finds in the magnetization up spectrum that the leading line is very strongly polarized, about -63% (- for minority, derived from the intensities in table 1). Also the second line for magnetization up shows a large polarization, but now of opposite sign, +77%. For the polarization integrated over the

Table 1: Binding energies and intensities of the components of spin-resolved Fe $2p_{3/2}$ spectra excited by circularly polarized light. The last line gives the overall spin polarization (- means minority spin type polarization).

BE (eV)	MAG +		
	maj	min	pol (%)
706.58	10.5	46.9	-63.3
706.85	14.6	1.9	+77.2
707.38	11.7	5.6	+35.1
708.00	4.1	4.7	-6.6
sum	40.9	59.1	-18.1
	100		
exp. total	**43.3**	**59.9**	**-16.1**

spectrum, the polarizations cancel partially, so that the overall polarization is -16.1%. So far, all core-level spectra measured show minority spin polarization within the peak region, consistent with the present finding.

Next we turn to the spin polarizations related to spin-orbit and exchange interaction. Both effects generate a photoelectron spin polarization by themselves, i.e. without the other one present, and they may enhance or suppress the spin polarization observed in a spectrum excited by circularly polarized light. This is evident in the different spin polarization (integrated over the photoemission peak) found with reversed sample magnetization or light helicity. The exchange polarization is obtained by classifying the spin-resolved spectra with respect to majority and minority. The remaining polarization of -13% does not contain the spin-orbit effect, and vanishes when the temperature is raised above the Curie point, i.e. it is related to the magnetism of the sample. It is caused by the exchange interaction of the core hole spin and the magnetically polarized valence electrons. In general, photoelectron spectra are influenced by diffraction of the photoelectrons by the crystalline surroundings of the emitting atom. However, we have shown in other spin-resolved dichroism studies that the exchange polarization is affected only very weakly by diffraction.

The spin-orbit polarization is obtained by classifying the spin-resolved spectra with respect to the spin direction imposed by the light helicity, i.e. by averaging out the effect of magnetization reversal. Since the polarizations observed for the two magnetizations differ, this would yield a finite result even if the sample was demagnetized. Therefore, it is an effect

caused by temperature-independent spin orbit (so) interaction, which can also be observed on non-magnetic materials, e.g. Cu [4]. In our experiment we found an so-polarization of -3%. Since magnetic dichroism and spin orbit polarization are closely related [5], there should be a sizeable so polarization. As a guide to the order of magnitude one may use the so polarization found in Cu metal as the basis for an estimate. This suggests an expected so-polarization of 15 to 20% for Fe under our experimental conditions. Photoelectron diffraction (PED) is unlikely to be the cause for the apparent disparity between magnetic dichroism and spin-orbit polarization since we know from linear dichroism [6] that PED scales spin-orbit polarization and magnetic dichroism in the same way depending on emission direction. Analysis of the data taking into account photoelectron diffraction in a multi-scattering approach is currently under way.

The results presented here show that the large width of the Fe 2p photoemission spectrum arises from the presence of discrete final states, which hitherto have not been observed unambiguously. The fact that *four* such final states can be identified is in agreement with a one electron model [7] in which the magnetically oriented valence electrons provide an effective spin field which splits the j = 3/2 states according to their m quantum number. However, the energy splittings and intensities cannot be described satisfactorily by such a model. Also, satellite states which are evident in the tails on the high binding energy sides of the spectra are (at present) beyond such a model. Interestingly, the lifetime broadenings of the majority and minority states appear to be similar. A

non-uniform splitting can be explained if the spin field is comparable to the spin orbit interaction (see figure 5 in ref. [5]). While this is plausible for the 3p level, the spin orbit interaction for the 2p shell is far too large for this explanation to hold [5, 8]. It is hoped that the present data will stimulate further theoretical investigations, which will account for sublevel energies and intensities. ■

REFERENCES

[1] L. Baumgarten, C.M. Schneider, H. Petersen, F. Schäfers, J. Kirschner, Phys. Rev. Lett. 65, 492 (1990).

[2] F.U. Hillebrecht, Ch. Roth, H.B. Rose, W.G. Park, E. Kisker, and N.A. Cherepkov, Phys. Rev. B 53, 12182 (1996).

[3] R. Jungblut, Ch. Roth, F.U. Hillebrecht, and E. Kisker, Surface Science 269/270, 615 (1992).

[4] Ch. Roth, F.U. Hillebrecht, W.G. Park, H.B. Rose, E. Kisker, Phys. Rev. Lett. 73, 1943 (1994).

[5] G. van der Laan, Phys. Rev. B 51, 240 (1995).

[6] H.B. Rose, T. Kinoshita, Ch. Roth, F.U. Hillebrecht, E. Kisker, Surf. Rev. Lett. 4, 915 (1997).

[7] H. Ebert, J. Phys. Condens. Matter 1, 9111 (1989); H. Ebert, L. Baumgarten, C.M. Schneider, J. Kirschner, Phys. Rev. B 44, 4406 (1991).

[8] J. Henk, A.M.N. Niklasson, B. Johansson, Phys. Rev. B 59, 13986 (1999).

HERCULES 2000

HIGHER **E**UROPEAN **R**ESEARCH **C**OURSE FOR **U**SERS OF **L**ARGE **E**XPERIMENTAL **S**YSTEMS

Grenoble, 27 February - 9 April 2000

• **Session A:** "Neutron and synchrotron radiation for physics and chemistry of condensed matter"
• **Session B:** "Neutron and synchrotron radiation for biomolecular structure and dynamics"

• **Hercules X EuroConference (6-9 April)**

Information: Secrétariat HERCULES - Marie-Claude SIMPSON
CNRS - Maison des Magistères. BP 166. 38042 Grenoble Cedex 9

Tel: 33 (0)4 76 88 79 86.
Fax: 33 (0)4 76 88 79 81.
E-mail: simpson@polycnrs-gre.fr
http: //www.polycnrs-gre.fr/hercules.html

Deadline for application: 15 October 1999

Fast Kinetics Study of Mesoporous Material Growth by Small-angle X-ray Scattering

F. Né[1],*, F. Testard[1], Th. Zemb[1] and J-M. Petit[2]

1 CEA Saclay, Service de Chimie Moléculaire, Gif sur Yvette (France)
2 ESRF, Experiments Division

The combined use of a stopped-flow apparatus, the high flux available on beamline ID2A at the ESRF and of a fast CCD camera allows the determination of real-time nucleation and growth processes of an organic/inorganic liquid crystal within a time range from 20 ms to a few seconds. These studies reveal microstructural mechanisms which are the key to synthesis of mesoporous materials.

Microporous materials such as zeolites are commonly used in industry as catalysts for chemical reactions and as molecular sieves for the separation of chemicals according to their molecular size. Zeolites, having pore sizes of less than 2 nm, are used to trap certain ions and very small molecules. Mesoporous materials, comparable to zeolites, have been of enormous interest since their discovery in 1992 [1] because their pore size is of the order of 2 to 50 nm in diameter, and thus they are able to accommodate larger molecules or complexed ions. Therefore, these materials have the potential for extending the fields of heterogeneous catalysis and separation. They could be used, for example, to increase the yield in the cracking process for asphaltenes, or as new molecular sieves for the separation of larger molecules [2].

Mesoporous materials are obtained by inorganic polymerization on the surface of direct micelles (often cationic surfactants). These micelles are destabilized by addition of a large quantity of inorganic multiply charged species, and in favorable cases, produce a well-organized hexagonal liquid crystal phase of closely packed charged apolar cylinders surrounded by polymerized inorganic oxide. In the final preparation step, the mixture is heated under hydrothermal conditions and the template is calcinated at high temperature. The final product shows a large specific area and exhibits a hexagonal order, as shown by small-angle x-ray scattering (SAXS) or by transmission electron microscopy (TEM) experiments.

The kinetic steps as well as the intermediate states are still unknown from the microstructural point of view in fast-growing organic-inorganic hybrid materials (formed "instantly" by precipitation). In the case of a slowly-growing (over a period of some hours) aluminosilicate zeolite, USAXS and WAXS, ultra small- and wide-angle x-ray scattering, experiments have been performed at the ESRF by T. Beelen [3], to provide evidence of the growth mechanism. In the case of mesoporous materials, some authors investigated the synthesis mechanism [2], but only a few of them concentrated on the very early stages of the formation of the material [4]. However, it seems to be in the very early stage that the final structure is determined, and therefore an understanding of the preorganization is relevant for control of the growth mechanism and hence also for control of the final structure and organization.

Our experiment has focused on the first preparation step of mesoporous zirconia. Two precursor solutions (in tanks S1 and S3) were mixed in a stopped-flow apparatus (Bio-Logic™), and pushed towards a 0.9 mm internal diameter quartz capillary located at the sample position on the high-brilliance SAXS beamline ID2A at the ESRF (Figure 1). The capillary was cleaned carefully between two mixing sequences by flushing with buffer (tank S2). 2-D scattering patterns were recorded by using the FRELON

CCD camera connected with a fast beam shutter (FBS). This setup allows very short exposure times of the order of 10 ms, following a minimum dead time of 6 ms (aperture of the FBS). The actual readout mechanism requires a minimum dead time of 0.4 s before the next acquisition. The dedicated stopped-flow software (Bio-Logic™) allows the definition of the desired acquisition start time for the mixing sequence. The flow rate is chosen for each motor to ensure a good mixing in the capillary before the acquisition starts.

Depending on the time-scale of the kinetics to be observed, we have adopted two experimental strategies:

a) "fast" kinetics measurements based on the following sequence: mixing, selecting as initial dead time

Fig. 1: Diagram of the stopped-flow apparatus. Stepping motors allow the choice of appropriate flow rates for mixing the components from the tanks S1, S2 and S3.
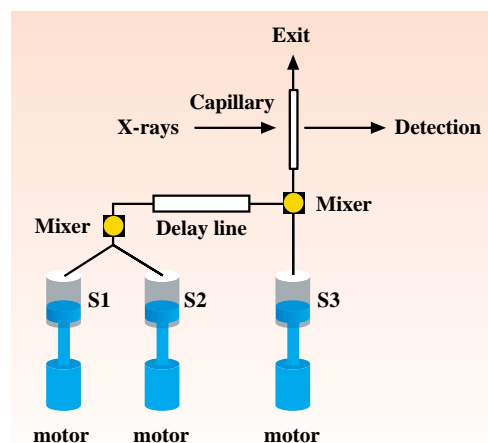
Fig. 2a: Typical intensity (I) obtained at the ESRF for a counting time of 10 seconds with a CTAB/zirconia mesoporous sample, after radial averaging and background subtraction. The Bragg peaks which provide evidence of the hexagonal structure have been indexed.
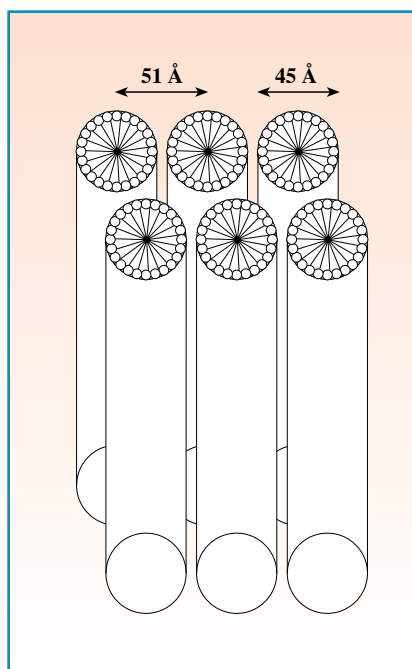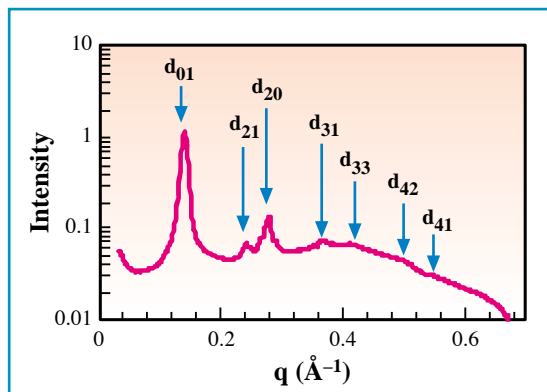

Fig. 2b: Schematic view of a hybrid liquid crystal. The surfactant cylinders are arranged in a hexagonal array; the polar volume within this hydrophobic template, covered by quaternary ammonium molecules, contains the zirconia network, which may lead to a mesoporous material after removal of the template.
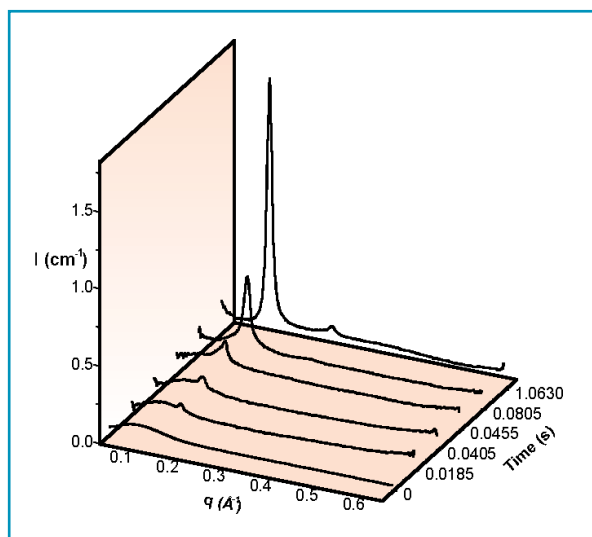

Fig. 3a: For fast kinetics experiments, SAXS patterns are recorded from 18 ms to 1 seconde, by changing the lowest initial dead-time. The first pattern (at 0 ms) corresponds to the one registered for the surfactant micellar solution as a reference.
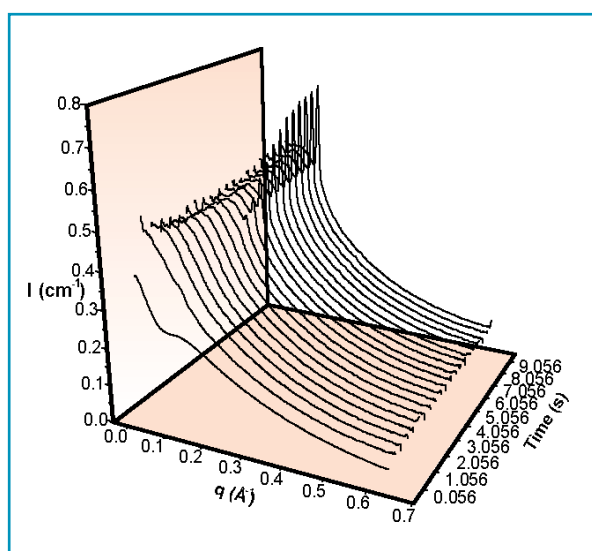
Fig. 3b: For the slow kinetics experiments, SAXS patterns were recorded from 56 ms to 10 seconds at 2 images per second. Here again, the first pattern corresponds to the initial solution of surfactant/$ZrOCl_2$ which was used as a reference.

the lowest one (6 ms), flushing and remixing with a longer dead time, again flushing, and so on.

b) "slow" kinetics measurements using a camera capable of recording two images per second, (lifetime of 0.1 s, separated by 0.4 s of dead time). The camera starts taking images just after the mixing.

For "fast" kinetics measurements, zirconium sulfate is used as the zirconium source. Two solutions are prepared, one containing 2.5 g of cetyl trimethyl ammonium bromide (CTAB) dissolved in 85 g water and one containing 4.55 g of $Zr(SO_4)_2$ dissolved in 15 g water. This procedure has been described previously by Ciesla et al. [5].

For "slow" kinetics measurements, the overall composition, by weight, of one stock solution is: 2.5 g of CTAB, 4.2 g of $ZrOCl_2$, and 100 g of H_2O whereas the other solution contains 18% by weight of $MgSO_4$ in water.

After mixing at room temperature, a typical SAXS pattern of a zirconia network, which had grown around cylinders of CTAB organized in a hexagonal array, was obtained (Figure 2a) in the q-range from 0.03 to 0.6 Å^{-1} (corresponding to Bragg spacings from 10 to 200 Å). This array of cylindrical templates are separated by a complementary volume containing all the polar components of the hybrid network of zirconia, surfactant counter-ions, water, and excess added salt. Since the distance between neighboring

cylinders is only 50 Å on average, the thickness of the zirconia walls, i.e. the distance of closest approach is only a few angstroms (Figure 2b). The second feature observable in the SAXS pattern is a broad form factor of zirconia species which are produced by the precursor particles.

Figure 3 shows the x-ray patterns obtained during both fast (a) and slow (b) synthesis. Growth of the Bragg peak intensity corresponded to the formation of the hybrid material. Since the Bragg peak was already at its final position in the first instants of detection and its width no longer continued to change, the growth mechanism should occur by a continuous process of inorganic oligomers feeding the growing microcrystal [6]. Moreover, at large angles, the patterns were superimposed, indicating that the size of the inorganic oligomers does not increase. Therefore, the solution behaves as a reservoir of micelles and of zirconia precursor nanoparticles.

For the fast synthesis, the first order appeared just after 18 ms. This is the shortest time we were able to achieve with our experimental configuration. This time results from the addition of the minimum dead time (6 ms) and half of the minimum acquisition time that we had chosen to get good statistics (25 ms).

For the slow synthesis, the peak appeared after 0.85 s. By increasing the temperature from 21°C to 50°C, the growth kinetics became much faster (the first order peak occurrence varied from 0.85 s to 0.056 s).

To determine the relevant kinetic parameters, we tried different concentrations of the surfactant and different counter ions. In the fast kinetics experiments, magnesium sulfate was added directly to the zirconium sulfate solution to vary the ionic strength of the reaction media. Figure 4 shows the increase of the maximum intensity of the first order versus time for two different concentrations of surfactant / $ZrOCl_2$ solution, for the slow kinetics experiments.

These examples show that determining reaction kinetics in organized molecular solutions with a resolution of 20 ms is feasible on ID2A, once equipped with a stopped-flow apparatus. We believe that this methodology offers the opportunity of new fast SAXS kinetics studies, since sources of parasitic background

Fig. 4:
Evolution of the maximum intensity of the first order step (slow kinetics experiments) for two different concentrations. Triangles: 300 μl of CTAB/$ZrOCl_2$/water solution (S1) and 60 μl of $MgSO_4$ solution (S3). Squares: 300 μl of CTAB/$ZrOCl_2$/water solution (S1), 360 μl of water (S2) and 60 μl of $MgSO_4$ solution (S3).
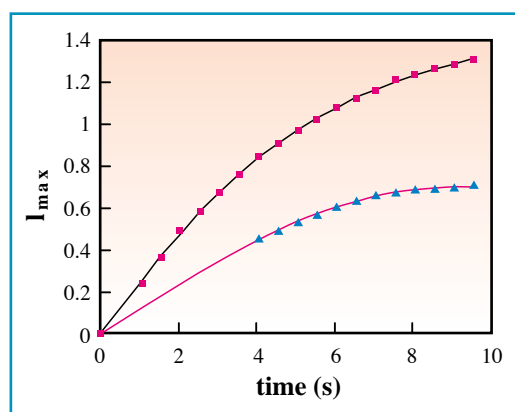
scattering, flux through sample, and dead time in the detection systems are easily recoverable at the ESRF. ■

REFERENCES

[1] *J. Beck, J. Vartuli, W. Roth, M. Leonowicz, C. Kresge, K. Schmitt, C. Chu, D. Olson, E. Sheppard, S. McCullen, J. Higgins, J. Schlenker, J. Am. Chem. Soc.,* **114**, *10834 (1992).*

[2] *Mesoporous Molecular Sieves, Proceedings of the first International Symposium, Studies in Surface Science and Catalysis, 117, Elsevier, Baltimore, July 1998.*

[3] *P. De Moor, T. Beelen, B. Komancheck, O. Diat, R. Van Santen, In situ investigation of Si-TPA-MFI crystallization using (ultra-) small- and wide-angle x-ray scattering techniques, J. Phys. Chem. B,* **101**, *11077, (1997).*

[4] *A. Monnier, F. Schüth, Q. Huo, D. Kumar, D. Margolese, R. Maxwell, G. Stucky, M. Krishnamurty, P. Petroff, A. Firouzi, M. Janicke, B. Chmelka, Science,* **261** *(Sept.), 1993.*

[5] *U. Ciesla, S. Schacht, G. Stucky, K. Unger, F. Schüth, Angew. Chem. Int. Ed. Engl.,* **35**(5), *541-543 (1996).*

[6] *Q. Huo, Chem. Matter.,* **6**, *1176 (1994).*

FURTHER REDUCTION OF EMITTANCE COUPLING

R. NAGAOKA, P. ELLEAUME, L. FARVACQUE, J.M. FILHOL AND A. ROPERT

ESRF, MACHINE DIVISION

The emittance coupling is defined as the ratio of the vertical emittance to the horizontal and should be as low as possible. It has recently been reduced at the ESRF by nearly a factor of three, achieving a record of less than 0.25%, thanks to new strategies based on response matrix modelling and x-ray pinhole measurements, introduced in this report.

One of the major performance enhancements to third-generation light sources such as the ESRF is the achievement of smaller transverse beam sizes, namely emittances, by orders of magnitude when compared with the previous generation. This comes from the fact that the brilliance of the photon beam is inversely proportional to the electron beam emittances. In the horizontal plane, in which the bending radiation occurs, the beam must be strongly focused to fight against the emittance growth due to the recoil of the photon emission. The focussing is obtained using a combination of quadrupole and sextupole magnets, called the "optics". These optics, which started by generating 7 nm·rad horizontal emittance, have furthermore evolved to achieve 3.7 nm·rad.

In the vertical plane, the emittance would ideally be zero. However, the inevitable magnetic imperfections in the storage ring give rise to the coupling mainly via the transfer of the horizontal betatron oscillation to the vertical. The generated coupling should therefore be corrected as much as possible. Since the relevant parameter for the beamlines is the actual vertical photon beam size, at the ESRF we derive the vertical emittance (and therefore the coupling) from the direct measurement of the photon beam size, using two x-ray pinhole cameras [1].

The principal source of the coupling is a skew quadrupole field, arising from a transversely tilted quadrupole magnet, or from a vertical orbit offset in a sextupole magnet. Efforts have been made to reduce the uncorrected coupling of around 10% ever since the commissioning stage. 16 skew quadrupole correctors introduced in the ring are tuned to compensate the two major resonances excited by the error sources; the difference ($Q_x - Q_z = 22$) and the sum resonances ($Q_x + Q_z = 51$), where Q_x and Q_z are the horizontal and the vertical tunes, respectively. The resulting coupling is reduced to less than 1%, which has been provided in the daily user service mode since 1995 [2].

RESPONSE MATRIX MODELLING

In developing a new correction scheme to proceed further, we have focused on orbit cross-talks, which are the orbit response in the plane perpendicular to the plane in which the orbit is shifted by a steerer magnet (Figure 1). While the direct response in the excited plane constitutes the diagonal response matrix, orbit cross-talks fill the off-diagonal part. Orbit cross-talks are generated by skew fields in a similar way as the coupling. The idea of using orbit cross-talks came from the fact that the aforementioned correction works well by starting from corrector values that give a reduced orbit cross-talk, as well as from the success of an accurate calibration of the quadrupoles with the diagonal response matrix. Thus the quadrupole strengths could be determined to 10^{-4} accuracy by analyzing measured matrices that consist of 224 BPM readings against each of the 96 steerer excitations (224 x 96 matrix in one transverse plane) [3].

Encouraged by this success, attempts were made to solve the equations for the unknown skew errors [4]. It must be noted that amplitudes of orbit cross-talks can only be a few tens of micrometers to stay in the linear optics regime. The present approach is therefore only applicable thanks to the excellent relative reading accuracy of the ESRF BPMs to a few micrometers, as well as to the precise knowledge of the quadrupole and the steerer calibration, obtained from the diagonal matrix analysis as stated above.

Despite finding that orbit cross-talks do not provide enough spatial resolution to identify a single quadrupole rotation, due primarily to the large scale of the ESRF machine, skew errors integrated over a certain longitudinal distance can be determined reliably. Several
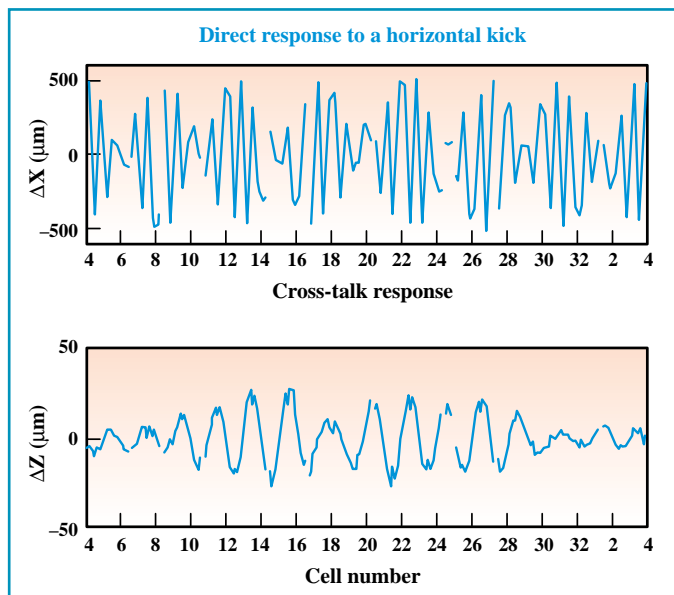

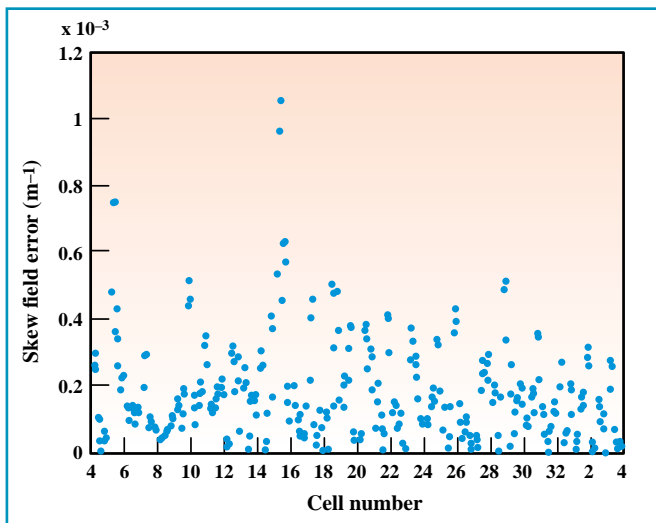*Fig. 1: An example of measured orbit responses.*

localized peaks are seen in the resulting error distribution (Figure 2). It was verified with the Alignment Group that the corresponding tilt angles are too large to be girder rotation errors. Challenging attempts shall be made by the Alignment Group to identify the skew field errors in the vicinity of the peaks and possibly to remove them. The measured tune separation around the difference resonance as well as the vertical dispersion are well reproduced with the obtained skew errors in the simulation [4]. The use of orbit cross-talks for the coupling analysis was also studied by the SOLEIL project team in collaboration, confirming the obtained result independently [5].

With non-uniformity revealed in the error distribution, a search was made for the most effective skew corrector positions. It was found that with a more symmetrical arrangement, the coupling can be reduced to less than 0.1% in the simulation, which led to 16 additional correctors being installed. As expected, actual application of the model solution led to a lower coupling than the standard correction. The remaining discrepancy with the predicted value is mostly attributed to inaccuracies in the analysis.

EMPIRICAL CORRECTION USING THE TWO X-RAY PINHOLE IMAGES

The best solution found in the simulation is expected to exist in the vicinity of the applied point. A difficulty was encountered here, however, that as a consequence of the reduced coupling, the orbit cross-talk is now too small to iterate the procedure. As the only

remaining yet promising alternative, use of the x-ray pinhole measurement was considered. The pinholes are capable of measuring the vertical emittance to less than 5 pm·rad [1]. The simulation finds that, starting from the model solution with proper weighting on the vertical dispersion, minimization of the vertical beam size measured at two locations in the ring (ID8 and D9) leads to the minimal coupling. It was in this way that the record value of 9 pm.rad, i.e. a coupling of less than 0.25%, was actually achieved as measured on both pinholes (Figure 3).
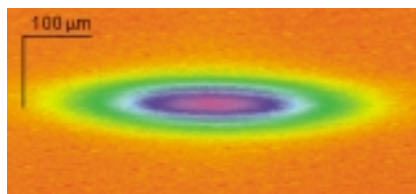

Fig. 3: The x-ray pinhole image (ID8 source point) at the smallest coupling (< 0.25%).

SOME ASPECTS OF THE ELECTRON BEAM AT THE SMALLEST COUPLING

It became clear, through the empirical corrections, that small vertical beam oscillations significantly disturb the beam size measurement as the coupling is reduced. The capability of varying the integration time between 20 to 1 ms in the pinhole measurement allowed the effect to be quantified. To fully benefit from small couplings, the vertical oscillations must be removed. The global orbit feedback plays an important role in suppressing the oscillations around 7 Hz,

which also aims to tackle the peak existing around 50 Hz in the near future. Notable progress is being made in parallel to reduce the vibration level of the girders with damping materials. Lifetime reduction for smaller couplings is found to be roughly up to 10 hours under the standard multibunch operation at 200 mA, in agreement with expectation. Although the sensitivity to insertion device gap variations increases for smaller couplings, it has been confirmed that an update of the empirical correction can well compensate their effects. An automatic correction procedure is foreseen.

CONCLUSION

The scheme developed to use the orbit cross-talk for the coupling analysis and the x-ray pinholes to reach the final minimum, along with the installation of new correctors, has successfully reduced the coupling of the ESRF machine by nearly a factor of three to less than 0.25%. With additional efforts either to damp the vertical oscillation or to eliminate the source, some further reduction could be attained. The first test beam delivery with the small coupling is scheduled for a limited number of shifts in October 1999. ∎

REFERENCES

[1] P. Elleaume et al., "Measuring Beam Sizes and Ultra-Small Electron Emittances Using an x-ray Pinhole Camera", J. Synchrotron Rad., 2, 209 (1995).

[2] ESRF Annual Report 1994/1995.

[3] L. Farvacque and R. Nagaoka, "Calibration of Quadrupole Magnets via Response Matrix Fitting", EPAC98, Stockholm, June 1998.

[4] R. Nagaoka, "Modelling of a Linearly Coupled Machine Using the Coupled-Response Matrix", EPAC98, Stockholm, June 1998; R. Nagaoka et al., "Correction of Linear Coupling on the Basis of Response Matrix Modelling and x-ray Pinhole Measurement", PAC99, New York, April 1999.

[5] P. Nghiem and M.A. Tordeux, "Coupling Correction for the ESRF", SOLEIL internal report, March 1999.

Events

13 years at the ESRF

Jean-Marie Lefebvre, Head of the Technical Services Division, retired thirteen years to the day since he joined the ESRF. He is pictured here, on the far right, during the early days with the directors of that era.

From left to right: A. Miller, W.D. Klotz, R. Haensel, B. Bach, J.L. Laclare, J.M. Lefebvre.

Left to right: D. Stuart, K. Wilson, P. Lindley; at the X-ray Damage Workshop.

Workshops

Three workshops were held at the ESRF in June: X-ray Damage to Crystalline Biological Samples; Biological Crystal Characterization; Pixel Detectors.

(See pages 3 to 5)

"HERCULES X EUROCONFERENCE"

Grenoble, 6-9 April 2000

Workshop devoted to

RECENT DEVELOPEMENTS AND APPLICATIONS OF NEUTRON AND SYNCHROTRON RADIATION

open to all HERCULES participants on the occasion of the 10th anniversary of the course.

Information:
Secrétariat HERCULES X EuroConference – Virginie GUERARD
CNRS - Laboratoire Louis Néel. BP 166. 38042 Grenoble Cedex 9
Tel: 33 (0)4 76 88 90 97. **Fax:** 33 (0)4 76 88 11 91. **E-mail:** guerard@polycnrs-gre.fr. **http:** //www.polycnrs-gre.fr/hercules.html.

Extended abstract and fellowship deadlines: 15 December 1999. Registration deadline: 31 January 2000.